Alma Mater Studiorum · Università di Bologna
Sede di Cesena

SECONDA FACOLTÀ DI INGEGNERIA CON SEDE A CESENA
Corso di Laurea Magistrale in Ingegneria Biomedica

Mathematical Modeling to Investigate Antiarrhythmic Drug Side Effects: Rate-Dependence Role in Ionic Currents and Action Potentials Shape in the O'Hara Model

Tesi di Laurea Magistrale in Bioingegneria Molecolare e Cellulare LM

Relatore:
Prof.
STEFANO SEVERI

Presentata da:
MARCO BUGANA

Correlatore:
Prof.
ERIC SOBIE

III Sessione
Anno Accademico 2010-2011

Happiness is not something ready made.
It comes from your own actions.
Dalai Lama

Alla mia famiglia

Abstract

Sudden cardiac death due to ventricular arrhythmia is one of the leading causes of mortality in the world. In the last decades, it has proven that anti-arrhythmic drugs, which prolong the refractory period by means of prolongation of the cardiac action potential duration (APD), play a good role in preventing of relevant human arrhythmias. However, it has long been observed that the "class III antiarrhythmic effect" diminish at faster heart rates and that this phenomenon represent a big weakness, since it is the precise situation when arrhythmias are most prone to occur.

It is well known that mathematical modeling is a useful tool for investigating cardiac cell behavior. In the last 60 years, a multitude of cardiac models has been created; from the pioneering work of Hodgkin and Huxley (1952), who first described the ionic currents of the squid giant axon quantitatively, mathematical modeling has made great strides. The O'Hara model, that I employed in this research work, is one of the modern computational models of ventricular myocyte, a new generation began in 1991 with ventricular cell model by Noble et al [31][49]. Successful of these models is that you can generate novel predictions, suggest experiments and provide a quantitative understanding of underlying mechanism. Obviously, the drawback is that they remain simple models, they don't represent the real system.

The overall goal of this research is to give an additional tool, through mathematical modeling, to understand the behavior of the main ionic currents involved during the action potential (AP), especially underlining the differences between slower and faster heart rates. In particular to evaluate the

rate-dependence role on the action potential duration, to implement a new method for interpreting ionic currents behavior after a perturbation effect and to verify the validity of the work proposed by Antonio Zaza using an injected current as a perturbing effect.

Keywords: action potential duration, arrhythmia, computational modeling, multivariable regression, reverse rate-dependence.

Riassunto

L'elettrofisiologia cardiaca è una disciplina che si è sviluppata nei primi anni 50 e che successivamente ha acquisito grande rilievo a livello di ricerca sperimentale. Grazie all'accoppiamento con la modellizzazione matematica è stato possibile raggiungere una comprensione quantitativa delle relazioni tra la funzione molecolare e il comportamento delle cellule miocardiche. A partire dal primo modello descritto da Hodgkin e Huxley (1952) sull'assone gigante di calamaro, la modellistica cardiaca ha fatto passi enormi, tanto che si parla di modelli di I e II generazione. Attraverso l'uso di questi modelli è stato possibile indagare più a fondo le aritmie cardiache, una tra le principali cause di morte nel mondo. Negli ultimi decenni è stato ampiamente verificato che l'azione dei farmaci anti-aritmici di classe III, i quali hanno il compito di prolungare la durata del potenziale d'azione cardiaco, presentano un grave effetto collaterale a frequenze cardiache più elevate, cioè proprio quando il loro effetto dovrebbe essere benefico. Questo problema prende il nome di *reverse rate-dependence*.

L'obiettivo che mi sono posto di raggiungere con questo lavoro di ricerca è stato quello di fornire ulteriori strumenti per approfondire il ruolo delle correnti ioniche che portano alla generazione del potenziale d'azione, in maniera tale da valutarne con maggior obiettività i differenti comportamenti a frequenze cardiache diverse.

A tal scopo ho utilizzato il modello matematico di cellula miocita ventricolare umana proposto da O'Hara et al. (2011). Per mezzo di questo modello è stato possibile: valutare l'efficacia dell'analisi di regressione multivariabile

sulla sensibilità dei parametri a una determinata uscita; valutare il ruolo della reverse rate-dependence sulla durata del potenziale d'azione; implementare un nuovo metodo per interpretare il comportamento delle correnti ioniche dopo l'effetto di una perturbazione; verificare la validità del lavoro proposto da Antonio Zaza sull'impiego di una corrente iniettata come effetto perturbante.

Acknowledgements

I would like to express my sincere gratitude to Professor Stefano Severi for this wonderful experience that has given to me. I'll never forget that november afternoon at the University when he told me:"Now you have to go..".

This study was carried out in the research group of Professor Eric. A. Sobie at the Department of Pharmacology, Mount Sinai School of Medicine, New York. I owe my deepest gratitude to Professor Sobie for the possibility to work under his professional supervision. I really appreciate the effort he put into planning this study and guiding me whenever needed, but also his trust by giving me the freedom and responsibility to do things and make decisions independently.

I wish to thank Eva, Amrita, Jhon, Frank and Young for the additional support during this study and for the collaboration. I am very grateful to Chiara, the best friend that I could find.

I would like to express my sincere gratitude to family Bortot (Peter, Michelle, Jennifer, Ashley, Duglas and "little" Marco). They have given me a great support and companionship during this study. They are my second family.

Contents

List of Figures

List of Tables

Chapter 1

Background

1.1 The cardiac action potential (AP)

Cardiac muscle tissue is formed from individual muscle cells, myocytes, bound to each other. For the contraction of a single myocyte, the chemical energy available in the myocyte in the form of adenosine triphosphate (ATP) has to be transformed into mechanical work to produce cell shortening. To produce coordinated forceful contraction of the whole tissue, this transformation must occur simultaneously in each myocyte of the tissue. The electrical signal is recruited as a rapidly deviating signal, which triggers the transformation of chemical energy into mechanical energy simultaneously throughout the whole tissue. The electrical signal propagates in cardiac tissue via gap junctions between cardiac myocytes. In each myocyte, the electrical signal initiates a process referred to as action potential. This signal may be recorded by means of microelectrodes. A typical action potential from a ventricular cell is diagrammed in Fig. 1.1.

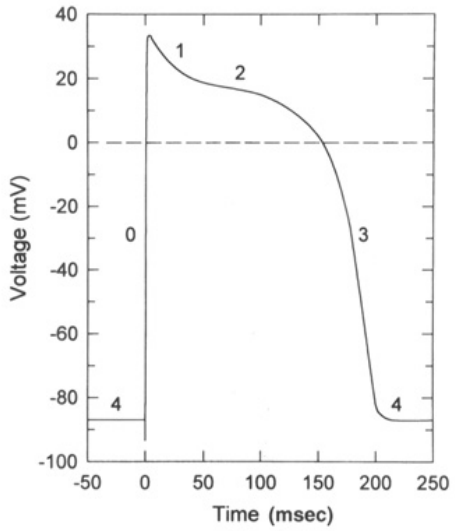

Figure 1.1: Typical action potential from a ventricular myocardial cell.

A cardiac action potential, once started in a cell, propagates by local current spread as in other excitable cells. A typical resting potential in a ventricular muscle fiber is -80 to -90 millivolts with respect to surrounding extracellular fluid.

1.2 Processes underlying the cardiac AP

To understand the basic mechanisms of ventricular arrhythmias and the single myocyte AP, we need to further deepen at the level of ion channel currents.
Currents that are actually responsible for the cardiac AP are basically two [7][9]:

(a) **inward currents**, that include voltage-gated Na^+ current (I_{Na}) responsible for the phase 0 depolarization and L-type Ca^{2+} current (I_{CaL}) responsible for maintaining plateau (phase 2) of the action potential; the inward component of electrogenic Na^+-Ca^{2+} exchanger may also contribute to the phase 2 of the AP.

(b) **outward currents**, that are mainly carried by different K^+ channels in human cardiac myocytes. They contribute to repolarization of different phases of the AP. These K^+ currents include the inward rectifier K^+ current I_{K1}, the transient outward K^+ current I_{to1}, the ultra-rapidly activating delayed rectifier K^+ current I_{Kur}, the rapidly and slowly activating delayed rectifier K^+ currents (I_{Kr} and I_{Ks}), acetylcholine-regulated K^+ current (I_{KACh}), and ATP-sensitive K^+ current (I_{KATP}).

The AP is determined by a balance of both types as a sequential activation and inactivation. An example of this balance is shown in Fig.1.2

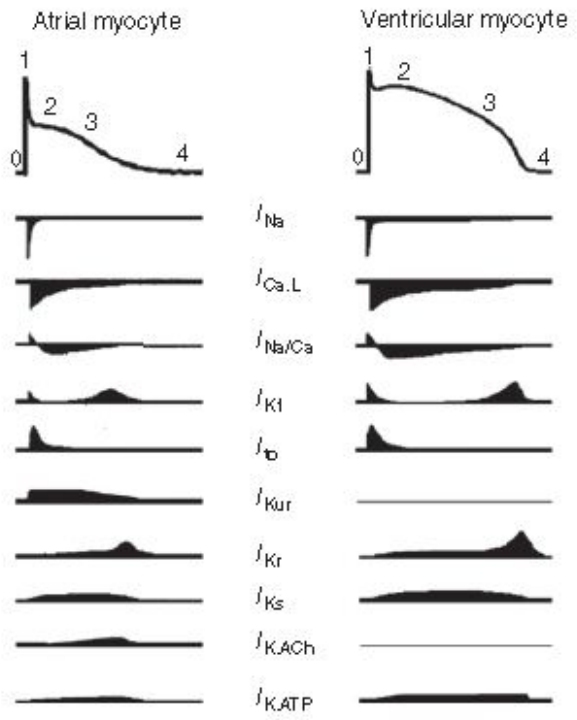

Figure 1.2: Time course of different ionic current contribution to human atrial and ventricular action potentials. The major ionic currents contribute to the AP shape at different phases. Downward plots represent the contribution to the AP of depolarizing inward currents; upward plots are the contribution of repolarizing outward currents.

The cardiac action potential duration (APD) may be 200-300 milliseconds (in contrast to 1 or 2 milliseconds for nerve and skeletal muscle), and it consists of 5 distinct phases (Fig. 1.1):

phase 0 – Depolarization The ionic mechanism underlying phase 0 depolarization in most cardiac muscle cells is a rapid (and transient) regenerative increase in sodium conductance G_{Na}. This permits the membrane potential to shift toward the sodium equilibrium potential (+40 mV). The fact that the action potential never reaches sodium potential (V_{Na}) reflects the residual permeability of the membrane to potassium. It has been shown that phase 0 is also accompanied by a fall in potassium conductance, with much slower kinetics.
It has been demonstrated that there is a second important inward (depolarizing) current which is activated by depolarization of the cell, the "slow inward current". This current is not sensitive to variations in extracellular sodium concentration, but is very sensitive to extracellular calcium concentration.

phase 1 – Repolarization Phase 1 repolarization is due primarily to a fall in sodium conductance.

phase 2 – Plateau The plateau (phase 2) is the most distinctive feature of the cardiac AP. During the plateau there is an approximate balance between inward-going calcium current and outward-going potassium current, and the membrane conductance is relatively low. The slow calcium current is the principal inward current during the plateau.

phase 3 – Repolarization Repolarization (phase 3) is a complex process which is not completely understood. Several mechanisms seem to be important. First, the potassium conductance increases, tending to repolarize the cell via a potassium-mediated outward current. The opening of these potassium channels is both time and voltage dependent: the potassium current

increases with time after the peak of the action potential even if Vm is held constant.

phase 4 – Resting potentials The resting potential (phase 4) in non-pacemaker cardiac cells is established by the same mechanisms as for other excitable cells. In the resting state the cell membrane is much more permeable to potassium than to the other ions. As a result, the resting potential is close to K^+ potential, typically -80 to -90 mV in ventricular myocardial cells.

1.3 Arrhythmias

The term "arrhythmia" usually describes an abnormal heart rhythm. Arrhythmias are called all conditions in which the origin, the regularity and the frequency of this electrical activity are altered (Fig.1.3). Abnormal automaticity is believed to be the result of reduced (more positive) resting membrane potential bringing it closer to the threshold potential. Ischemia and electrolyte imbalances are two causes of reduced membrane potential that may result in abnormal automaticity.

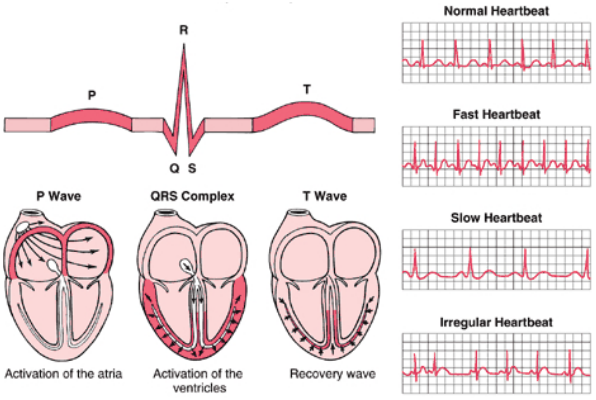

Figure 1.3: On the left, illustration of the relation between the AP propagation and the QRS-T at baseline; on the right, example of normal heartbeat and simple arrhythmias.

Heart's electrical system To understand arrhythmias, it helps to comprehend the heart's electrical system. The heart performs its pumping function by contracting rhythmically with a frequency of about 60-90 beats per minute. At the base of the contraction there is an electrical stimulation of the cardiac cells. This is determined by a real electric current that runs through the heart with each beat, stimulating the contraction. This stream originates from a well-defined center of the heart, located in the right atrium and called the sinoatrial node, and has a course equally well defined. In fact, it active before the atria and, subsequently, through a series of structures that form a single conduction pathway, activates the ventricles (Fig. 1.4).

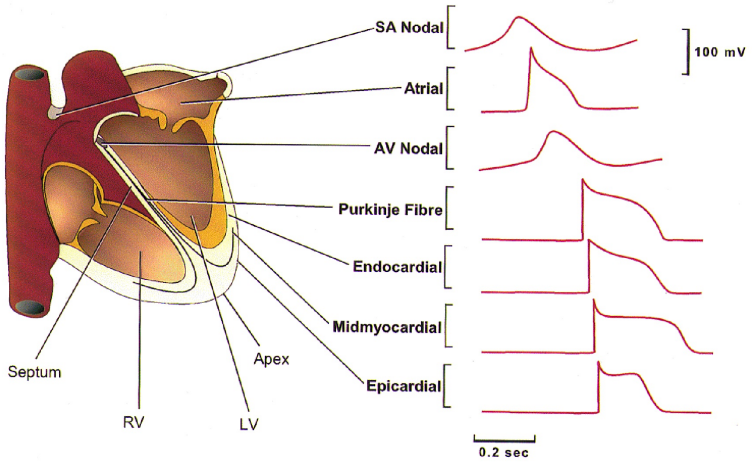

Figure 1.4: Examples of the various action potential waveforms throughout the cardiac conduction and contractile systems. (Nerbonne, 2000)

Arrhythmias classification There are several ways to classify arrhythmias, nevertheless the first and most important distinction can be made between:

1. tachyarrhythmias, characterized by a frequency of the pulses increased;
2. bradyarrhythmias, characterized by a reduced frequency of the pulses.

The most serious ventricular arrhythmia is the ventricular fibrillation that causes the death of more than 400,000 people in the USA annually. The most

common arrhythmia, instead, is the atrial fibrillation, that is indirectly a life threatening disease [13].
Arrhythmias can recognize many causes. Sometimes they are secondary to structural heart disease, other times it may be due to extra-cardiac diseases. Nevertheless, many arrhythmias can occur in an apparently healthy heart and in the absence of other pathologies.

Drug side effects Many drugs are used in the treatment of tachyarrhythmias. In many cases they allow effective prevention of recurrence; however, these drugs may be burdened by important side effects. Spontaneous depolarizations requiring a preceding impulse (a triggering beat) are called afterdepolarizations (or triggered activity). If afterdepolarizations originate during phase 2 or 3 of the monophasic AP they are classified as early afterdepolarizations (EADs) (Fig. 1.5). A consequence of early afterdepolarization (EAD) is drug induced Torsade de Pointe (TdP), a polymorphic form of ventricular tachycardia that is a potentially lethal complication of anti arrhythmic and other drugs that prolong the QT-interval. Afterdepolarizations originating from phase 4 of the AP are classified as delayed afterdepolarization (DAD) (Fig. 1.6).

Among the currents illustrated above, cardiac K^+ channels play a crucial role in the AP regulation, as important targets of antiarrhythmic drugs. The most important functions of these currents are essentially three: regulate the resting membrane potential, participate in the repolarization and determine the AP shape and the APD. A malfunction of them causes an alteration of the electrical balance of depolarization and repolarization, and therefore an alteration of the balance between inward and outward currents.
The delayed rectifier K^+ current (I_K), a key outward current for cardiac repolarization (as described above), is comprised of rapid (I_{Kr}) and slow (I_{Ks}) components with distinct rectification characteristics, kinetics and drug sensitivities. I_{Kr} block has been the major target for most class III antiar-

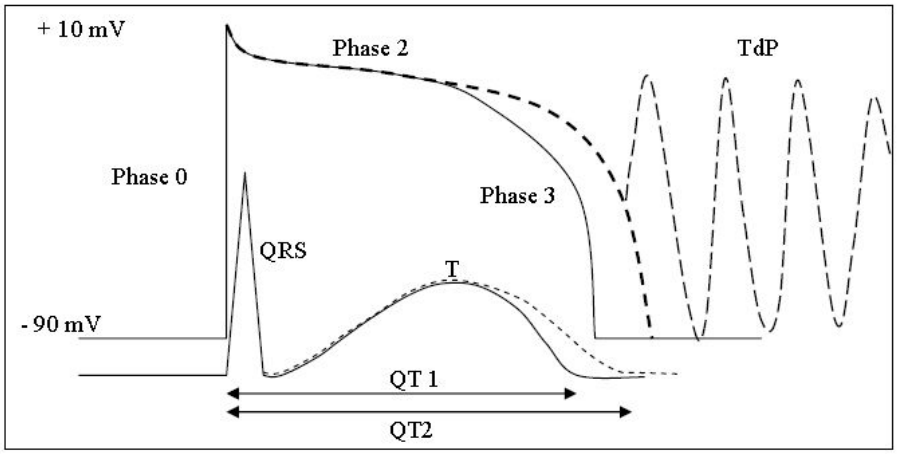

Figure 1.5: Torsade de pointe, a potentially lethal polymorphic ventricular arrhythmia, is a consequence of EAD; it may be precipitated by potassium channel blockers.

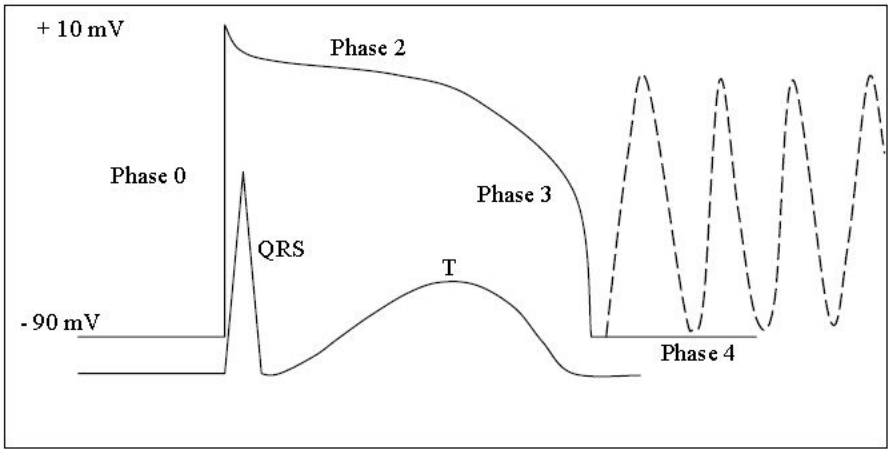

Figure 1.6: Triggered activity originating from phase 4 of the AP. This is known as delayed afterdepolarization (DAD)

rhythmic agents (e.g. dofetilide, sotalol, E-4031), which exert their effects by prolonging cardiac action potential duration (APD) and refractoriness. However, the usefulness of these agents is limited by their undesirable reverse rate-dependent profile: excessive drug effects at slow heart rate or long

diastolic interval, but loss of efficacy at fast heart rate [15]-[19].

1.4 The reverse rate-dependence (RRD)

The loss of class III effect with increasing cardiac frequency has been termed "reverse rate-dependence". The RRD is the inverse proportionality between drug-induced APD modulation and heart rate. Electrophysiologic studies have demonstrated that sensitivity of APD to perturbations and modulating factors is larger at slow rates or, more in general, when repolarization is initially slow [3].

1.5 Why is reverse rate-dependence bad?

The RRD is undesirable because it minimizes drug effects on repolarization during tachyarrhythmias. Class III anti-arrhythmic agents action is usually caused by blockade of one or more potassium channels [2][9]. Several hypotheses are explained by the following issues:

- the significant accumulation of I_{Ks} may occur due to the incomplete deactivation of the current at fast heart rates, which would greatly attenuate the APD lengthening effect of I_{Kr} blockade;

- the effect of I_{Kr} blockers is reduced (and consequently the drug-induced prolongation of APD becomes diminished) at fast heart rates due to the potassium accumulation in the sarcolemmal clefts;

- the rate-dependence of drug-channel interaction;

- I_{Kr} and I_{K1} interact with rate-dependent changes in repolarization in a way potentially contributing to RRD.

Nevertheless an effect on inward currents or ion pump mechanism can not be entirely excluded. Thus, It is evident that the exact mechanism of the RRD is still unclear, especially with the multitude of concerned ionic currents.

1.6 Zaza's hypothesis for RRD

Assuming that the complexity of the mutual interplay between membrane potential course and the ionic currents can still hold secrets, in a recent publication Zaza studied this interplay from two viewpoints: how membrane current sets membrane potential course and how membrane potential course may, in turn, affect individual channel activity.
In particular he studied the role of membrane potential velocity in determining reverse rate dependency of drug effects on APD and in exposing "non-equilibrium" phenomena in channel gating [3]. His results are shown in Fig.1.7, where the calculated APD prolongation caused by adding a constant I_m is remarkably larger for the AP recorded at the slower pacing rate.

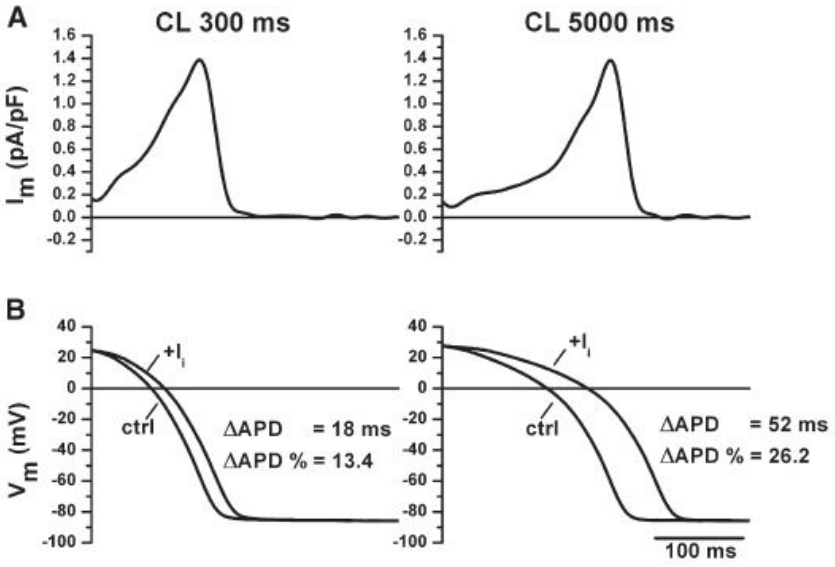

Figure 1.7: Results of Zaza's experiments. Numerical reconstruction of RRD of APD prolongation induced by a change in I_m. Zaza injected a constant current I_i=-0.05pA/pF at pacing cycle lengths of 0.3 (left) and 5 s (right). (A) dVm/dt and corresponding I_m traces. (B) Repolarization time courses in control (ctrl) and during I_i injection ($+I_i$) back-calculated by numerical integration from the original and modified dVm/dt traces respectively. ΔAPD is APD prolongation (at 90% repolarization) induced by I_i. Cm = 100 pF used for all conversions between dVm/dt and I_m.

He showed that RRD of APD prolongation does not require RRD of changes in membrane current I_m. In other words, his idea of "intrinsic reverse rate-dependence" is that shorter APs (at fast rates) will have faster rates of repolarization, and therefore if you try to extend this, for instance by injecting a current, this will have a smaller effect at a faster rate compared with that of a slower rate.

1.7 Mathematical modeling

Using ionic models it is possible to simulate the dynamics of wave propagation in human ventricular tissue and studying the stability of reentrant waves and their relation to arrhythmias. In addition it is important to reproduce key characteristics such as the rate-dependence of action potential duration (APD) and also tissue-level characteristics that are important for describing correct wave propagation and dynamics. Through these models it is possible to reproduce action potential (AP) morphologies accurately in tissue because it is known that electrotonic currents modify the APs produced by isolated cells, potentially altering the AP amplitude and affecting the relationships among the transmembrane currents.

1.7.1 Mathematical modeling purpose

The primary purpose of mathematical modeling and computer simulations of mathematical models is to explain how the studied systems work. Using mathematics it is possible to integrate experimental data from the studied system and previous theories into a single context, which explains how the system works (Fig. 1.8). With modeling it is also possible to extrapolate how the system would function in a different environment and with different features. Part of the real life experiments can thus be replaced with model simulations of the studied system. Parameters and interrelationships, which are hard or impossible to measure from the studied system, can also be estimated with modeling. Modeling becomes very useful especially when the complexity of the system increases beyond our capability to understand it directly.

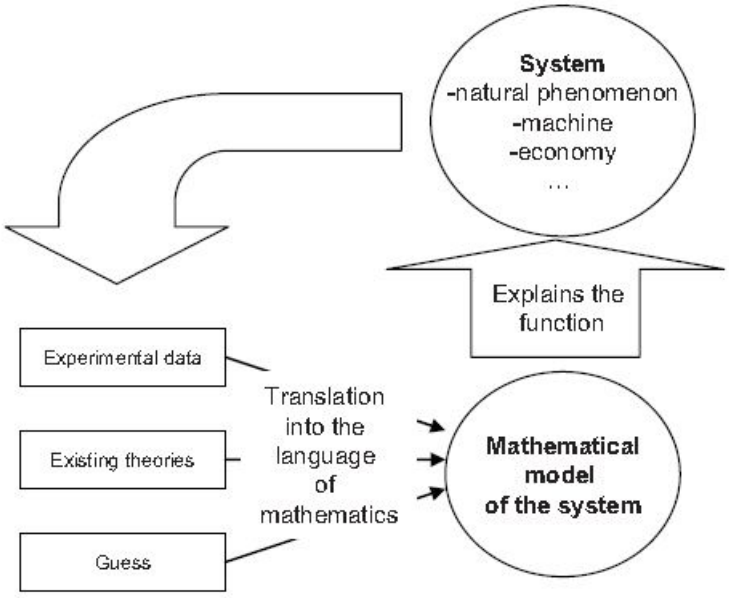

Figure 1.8: Mathematical modeling diagram. Mathematical modeling is used to explain and describe how systems work.

The downside of mathematical modeling, clearly, is that it is only a model, not the real system; moreover models include approximations and guesses. Thus, use of these models to predict alterations of AP repolarization due to drugs or diseases should be made with caution. Nevertheless, with the introduction of many of these models in their original form, new information regarding human myocytes electrophysiology has become available. In biology and physiology and furthermore in excitation-contraction coupling (ECC) studies, mathematical modeling has become an essential part of the research methodology with an increasing trend [37][30][31].

1.7.2 Mathematical modeling of cardiac cells

To study cellular cardiac electrophysiology in a range of disease states, in the past years several mathematical models were created [31]. The goal of these models has been to achieve a quantitative understanding of the relationships between molecular function and the integrated behavior of the

cardiac myocyte in health and disease. The most important issues of these models were:

- to quantify the importance of individual K^+ currents for AP repolarization;
- to understand the role of the rate-dependence of AP prolongation upon K^+ channel block;
- to find the cause of APD shortening at faster heart rates.

1.7.3 History of mathematical modeling

The first step towards mathematical modeling of cardiac ECC was made in the area of AP modeling, when Hodgkin and Huxley presented the mathematical description of ion currents generating APs in the squid giant axon [32]. This model-based description of the sodium, potassium, and leakage (chloride) ion channels in a squid axon used first-order kinetics (with voltage-dependent rate constants) for the time-dependent gates controlling the flow of ions across the cell membrane. The Hodgkin-Huxley (H-H) equations were later introduced to the field of cardiac APs [33], and the H-H formalism is still used as a part of nowadays AP modeling [34][30][35][36]. In addition to AP modeling, the work of Hodgkin and Huxley stands out in biology as one of the most successful combinations of experiment and theory [37].
Since that time, the number of different cell models has grown rapidly as more has become known about the different subcellular mechanisms responsible for the functioning of the cell. The role of intracellular Ca^{2+} and its underlying mechanisms began to be revealed in the 1970s and 1980s [30][38]. In 1975, McAllister et al. published a cardiac action potential model of Purkinje fiber composed of nine ionic channels [50]. This model described for the first time the role of Ca^{2+} during the generation of action potential. The model consists of a rapid inward Na+ current (INa), a secondary inward current (ICa), a transient chloride current (ICl), a time-independent K+ current (IK1), a transient K+ current (IK2), and the fast (IX1) and slow (IX2)

components of a new current. However, modeling did not change completely from AP modeling to ECC modeling. In addition to complete ECC models, sole AP models with no or very simplified intracellular Ca^{2+} dynamics are still used nowadays.
After the mid-1990s, modeling moved from general models towards species-dependent models, which is reasonable due to the large differences in ECC between different species [34][30]. Single cell ECC modeling has also been used as a sub-model in generating tissue-level phenomena [35]. On the other hand, local-control theory introduced a completely new accuracy scale to the modeling and understanding of intracellular mechanisms in ECC [41]. Some of the better-known models include the DiFrancesco-Noble model [40] of the Purkinje fiber cell, the Beeler-Reuter ventricular cell model [39], the Luo-Rudy mammalian ventricular cell models [42][43], and the Noble model [44] of the guinea pig ventricular cell.

1.8 Multivariable regression analysis

Parameter sensitivity analysis is the process of determining the sensitivity of responses to the change of parameter values [51]. It has been introduced as a powerful tool for systems biological approaches due to its practical applicability to model building and evaluation, understanding system dynamics, evaluating the confidence of a model under uncertainties, and experimental design [52][53]. However, often the choice of parameters appears to be critical: different parameters configurations could produce virtually identical outputs morphology. An example is shown in Fig.1.9.

Based on this problem, multivariable regression has been introduced as a powerful tool to systematically analyze mathematical models of heart cells due to its practical applicability to model building and evaluation, understanding system dynamics, evaluating the confidence of a model under uncertainties, and experimental design.
The multivariable regression technique, used in this research, refers to partial

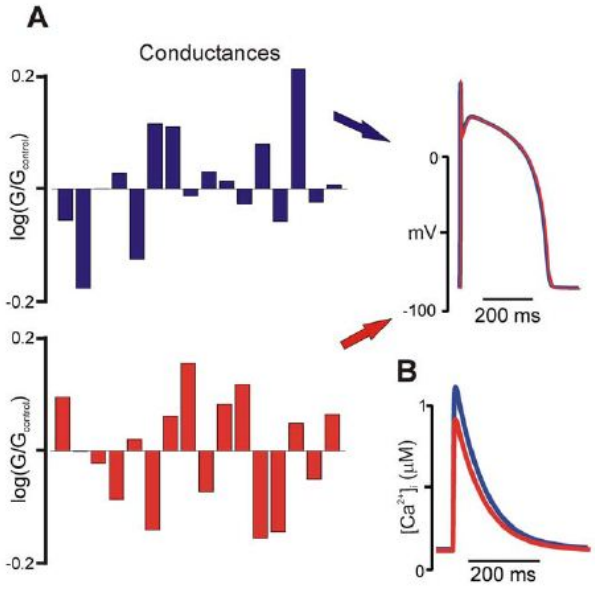

Figure 1.9: Parameter variation effects on model output. Different combinations of parameters (e.g. conductances) produce nearly identical outputs morphology: (A) action potential and (B) intracellular calcium Ca^{2+} transient.

least square (PLS) regression, particularly useful when we need to predict a set of dependent variables from a (very) large set of independent variables (i.e., predictors)[14]. The goal of PLS regression is to predict Y from X and to describe their common structure. If Y is a vector and X is a full rank matrix, this goal could be accomplished using ordinary multiple regression. When the number of predictors is large compared to the number of observations, X is likely to be singular and the regression approach is no longer feasible.

Each input matrix X has dimensions $n \times p$, where n is the number of sets of random parameters, and p is the number of model parameters varied. Each output matrix Y has dimensions $n \times m$, where m is the number of outputs. PLS regression produces a matrix B_{PLS} of regression coefficients ($p \times m$). This procedure generates a simple empirical model that can predict the outputs resulting from a new set of input parameters through the formula

$Y_{predicted} = X \times B_{PLS}$ (Fig.1.10). The regression coefficients in the matrix

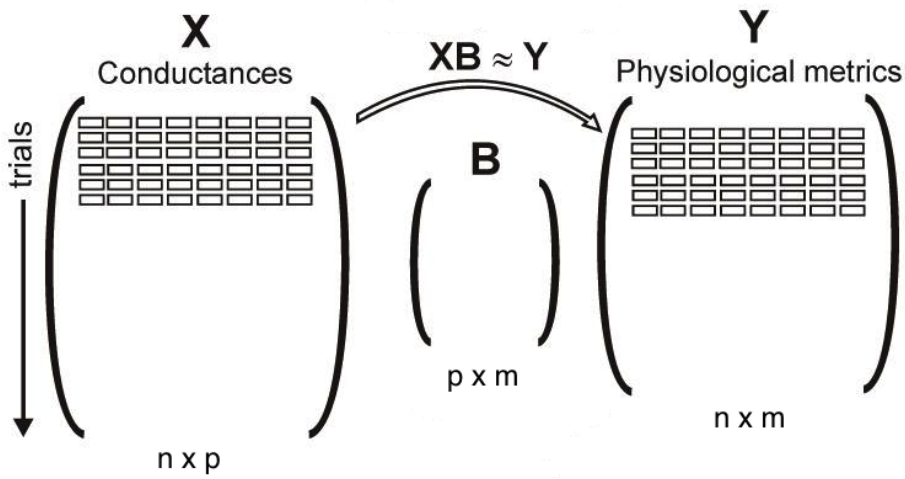

Figure 1.10: Schematic of input (X), output (Y), and PLS regression matrix (B_{PLS}) structures.

B_{PLS} indicate how changes in input parameters lead to changes in outputs, with each column reflecting the effects on a particular output. Examining these coefficients allows for an assessment of the relative contributions of the various parameters.

In the results presented here, parameters were varied independently, and numerous trials were run to obtain an accurate estimate of B_{PLS}. All matrices used for regression therefore had full rank. Because of this, the results obtained using the PLS regression were identical to those that would have been obtained using more traditional multivariable linear regression. For instance, B can be computed from the formula $B = (X^T \times X)^{-1} \times X^T \times Y$, where the superscript T denotes the matrix transpose, and the superscript -1 indicates the inverse of a square matrix. PLS regression, rather than standard multivariable regression, was used because this technique can be applied even when the number of variables is much greater than the number of samples (i.e., $p > n$). In such a situation, the standard regression formula could not be used because the matrix $X^T \times X$ would be singular.

Chapter 2

Aims of the Research

Mathematical modeling has proven its usability in studying excitation-contraction coupling in cardiac muscle cells. However, behaviors of specific ionic currents after a perturbation is not understood quantitatively, especially when we talk about issues of the drug-induced prolongation of the electrocardiographic QT interval.

The purpose of the present research is to give an additional tool in understanding the rate-dependence role in the O'Hara model and to study how a perturbation can influence ionic currents and action potential shape and if this influence could be forward rate-dependent, reverse rate-dependent, or rate-independent. The specific issues are:

1. to test and confirm the efficiency and usability of multivariable regression with the O'Hara model;

2. to find a method that can help to understand what currents combinations are responsible for cardiac arrhythmias;

3. to test and confirm Zaza's hypothesis.

Chapter 3

Materials and Methods

Simulations were performed with the O'Hara model, which was used to describe cellular electrophysiology mechanisms specific to human ventricular myocytes [24].

3.1 O'Hara model

The model is essentially based on data from human ventricular myocyte experiments and simulates the major ionic currents and fluxes, based either directly or indirectly on undiseased or non-failing human experimental data. It is able to reproduce heterogeneity in human epicardial, endocardial and myocardial cell action potentials. The endocardial myocyte was considered the baseline model in the simulations. It was proposed by O'Hara et al. for understanding the basic mechanisms of ventricular arrhythmias at the level of ion channel currents and the single myocyte AP. It is referred to the ORd (OHara-Rudy dynamic) model.

To keep the ORd model computationally efficient and parameters well constrained, the Hodgkin-Huxley formalism was used in formulating current equations. This choice was made as a design principal with the thought that interested users can modularly replace any current or flux with more detailed Markov formulations of mutation or drug effects as desired (e.g.[25][26]). Sim-

ilarly, intracellular Ca^{2+} handling can be modified (e.g. more spatial detail, Markov ryanodine receptor implementation), or various signaling pathways and related effects on ion channels can be added [27][28][29]. The basic ORd model has 41 state variables (Tab. A.1, A.2, A.3). In the absence of CaMK (Ca^{2+}/calmodulin-dependent protein kinase II) and its effects on target currents and fluxes, the number of state variables is 31. Fig.3.1 illustrates a schematic diagram of the O'Hara model.

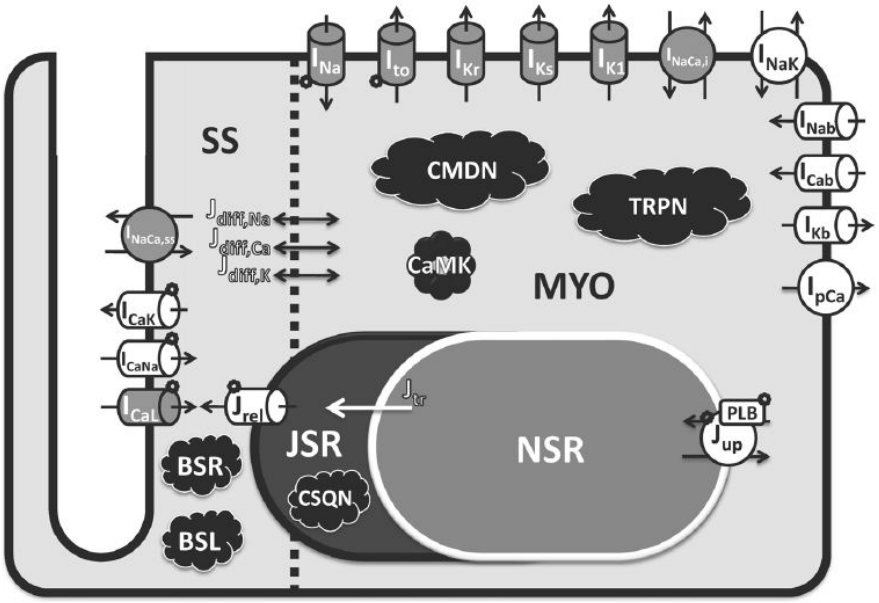

Figure 3.1: Schematic diagram describing ionic currents, pumps, and exchangers that are captured in the of O'Hara human ventricular myocyte model.

This mathematical model consists of four compartments:

(1) bulk myoplasm (MYO);

(2) junctional sarcoplasmic reticulum (JSR);

(3) network sarcoplasmic reticulum (NSR);

(4) subspace (SS), the space near the T-tubules.

ORd equations are all smoothly varying functions, free of singularities and if conditionals. Thus, the model can readily be implemented in any of a variety of automated numerical integrators, such as Matlab. Currents into the myoplasm are:

- Na^+ current (I_{Na}), representing both fast and late components;
- transient outward K^+ current (I_{t0});
- rapid delayed rectifier K^+ current (I_{Kr});
- slow delayed rectifier K^+ current (I_{Ks});
- inward rectifier K^+ current (I_{K1});
- 80% of Na^+/Ca^{2+} exchange current ($I_{NaCa,i}$);
- Na^+/K^+ pump current (I_{NaK});
- background currents (I_{Nab}, I_{Cab} and I_{Kb})
- sarcolemmal Ca^{2+} pump current (I_{pCa}).

Currents into subspace are:

- L-type Ca^{2+} current (I_{CaL}, with Na^+ and K^+ components I_{CaNa}, I_{CaK});
- 20% of Na^+/Ca^{2+} exchange curent ($I_{NaCa,ss}$).

Ionic fluxes are:

- Ca^{2+} through ryanodine receptor (J_{rel});
- NSR to JSR Ca^{2+} translocation (J_{tr});
- Ca^{2+} uptake into NSR via SERCA2a/PLB (J_{up}; PLB-phosspholamban);
- diffusion fluxes from SS to myoplasm ($J_{diff,Na}$, $J_{diff,Ca}$ and $J_{diff,K}$).

Ca^{2+} Buffers:

- calmodulin (CMDN);
- troponin (TRPN);
- calsequestrin (CSQN);
- anionic SR binding sites for Ca^{2+} (BSR);
- anionic sarcolemmal binding sites for Ca^{2+} (BSL).

Initial Conditions used during simulations are:
V=-87 mV; Na_i=7 mM; $Na_{ss} = Na_i$; K_i=145 mM; $K_{ss} = K_i$; Ca_i=1.0e-4 mM; $Ca_{ss} = Ca_i$; Ca_{nsr}=1.2 mM; $Ca_{jsr} = Ca_{nsr}$; m=0; h_f=1; h_s=1; j=1; h_sp=1; j_p=1; m_L=0; h_L=1; hL_p=1; a=0; i_F=1; i_S=1; ap=0; iFp=1; iSp=1; d=0; ff=1; fs=1; $fcaf$=1; $fcas$=1; jca=1; nca=0; ffp=1; $fcafp$=1; xrf=0; xrs=0; $xs1$=0; $xs2$=0; $xk1$=1; J_{relnp}=0 mM/ms; J_{relp}=0 mM/ms; $CaMKt$=0;

3.2 Regression analysis

At the beginning, I changed the O'Hara model from the original MATLAB code to a new version, similar to the one generally used at Sobie laboratory (Mount Sinai School of Medicine, New York, NY, USA). These changes are:

- to create two MATLAB files .m, *dydt_ohara* and *ohara_ode* (main file). In the *dydt_ohara* function all the currents are defined and the Action Potential is calculated; *ohara_ode* is the main file where the differential equations of the *dydt_ohara* are solved by the ordinary differential equations (ODEs), in particular ode15s of MATLAB numerical integration;
- to define all constants *global* at the beginning of the *ohara_ode* file;
- to set the initial conditions;
- to define the simulation, the stimulus and recording parameters;

- to plot the last AP and all the currents.

Stimulus The stimulus was the result of three times (Appendix **??**):

1. time of delay before the stimulus;
2. time during the stimulus;
3. time after the stimulus.

Parameter randomization In regards to the parameters, I set up a loop that randomizes them:

$$G_{scaling} = e^{\sigma \times randn(nG_x)}$$

where $\sigma = 0.1823$ and nG_x is number of the conductances to vary.

Multivariable regression Therefore I computed the multivariable regression. The baseline parameters were randomly varied hundreds of trials in order to generate an "input" matrix **X**. Using this input data set, simulations were performed under identical conditions to measure the APD and the calcium transient. These two quantities were collected in the "output" or **Y** matrix for each of the trials. The multivariable regression was then used to compute a matrix **B** whose elements indicate how changes in input parameters, namely maximal ionic conductances (Tab.A.2), kinetic parameters (p-values, Tab.A.1) and the voltage dependences of activation and inactivation (V-shifts, Tab.A.3), affect the model outputs. Fig.3.2 shows a schematic representation of multivariable regression.

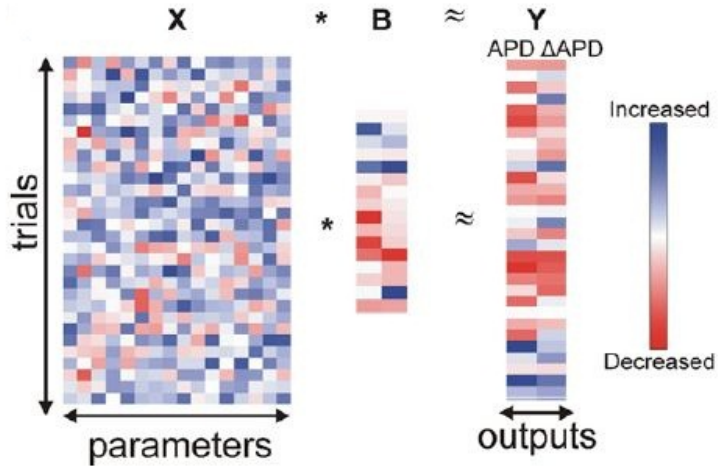

*Figure 3.2: Schematic representation of multivariable regression. Model parameters (**X**), simulation results (**Y**), and parameters sensitivities (**B**) are collected in matrices with the indicated structures and relationships. Values in matrices are represented using the indicated color table.*

Outputs of the model Initially, I studied four outputs: the action potential duration (APD), the resting membrane potential (V_{rest}), peak voltage during the AP (V_{peak}) and the calcium handling ($\Delta[Ca^{2+}]_i$). The APD was defined as the time from the maximum upstroke velocity (dV/dt_{max}) to the -60mV crossing; the Ca^{2+} was calculated as the transient amplitude ($\Delta[Ca^{2+}]_i$), defined as peak intracellular Ca^{2+} minus the level immediately before the AP.

The input matrix **X** was generated by randomly varying 42 parameters comprising 14 conductances (Gs), 18 p-values that multiply the gating variable time constants and 10 V-shifts values that change the voltage dependence of activation or inactivation. Random scale factors for conductances and time constants were chosen from a log-normal distribution with a median value of 1 so that the probability that a conductance was doubled equaled the probability that its value was halved. This was done to eliminate the possibility of being left with non physiological conditions of a negative conductance or

negative time. The standard deviation (σ) of log-trasformed variables controlled extent to with parameters varied and was set to 0.1823 in the case of both the conductances and the p-values. This means that an increase of 20% represents one standard deviation away from the control value ($e^{0.1823} = 1.2$). Shifts of the gating variable infinity curves along the voltage axis could be positive or negative. These random variables were normally rather than log-normally distributed and the values of σ was set to 2 mV.

A total of 300 trials random sets of parameters were generated such that $\mathbf{X}$ had dimensions 300×42. To compute the output matrix $\mathbf{Y}$, simulations were performed with each of the 300 models defined by a given parameter set. The four outputs constitute the four columns of the 300×4 $\mathbf{Y}$ matrix (Fig.3.3). The first column of $\mathbf{Y}$ contains the APD measured as the time from the upstroke to the -60 mV crossing and computed after applying 100 stimuli at 2 Hz; the second contains V_{peak}; the third contains V_{rest}; the last one corresponds to $\Delta[Ca^{2+}]_i$, maximum $[Ca^{2+}]_i$ minus minimum $[Ca^{2+}]_i$.

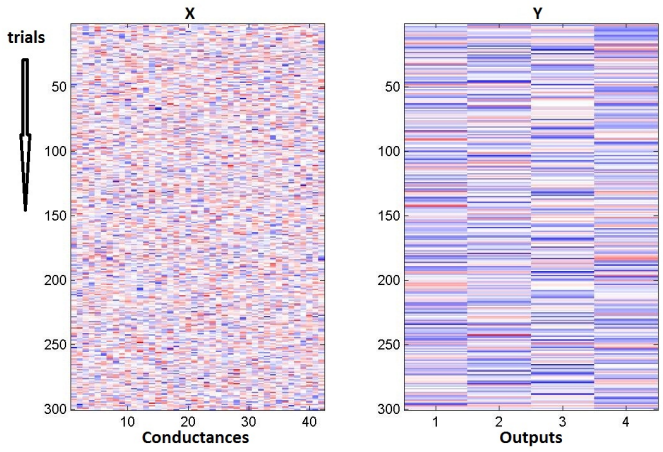

*Figure 3.3: Multivariable regression. Model parameters (**X**) and simulation results (**Y**) are collected in matrices with the indicated structures. Blue is positive value, red is negative value. These two matrix are related by the matrix of parameters **B**, where each row represents the contributions of each of the conductances to a particular output.*

Since **X** and **Y** contained quantities in different units, these values were converted into unit-less z-scores, i.e. each column was mean-centered and normalized by its standard deviation. Finally, multivariable regression was performed in order to build a linear model relating the input and output matrices as per the relation $X \times B = \hat{Y}$, where **B** is a matrix of regression coefficients and $\hat{Y}$ is a close approximation of **Y**.
An example of matrix **B** and how a change in the input parameters causes a change in two outputs (APD and $[Ca^{2+}]_i$) is shown in Fig.3.4.

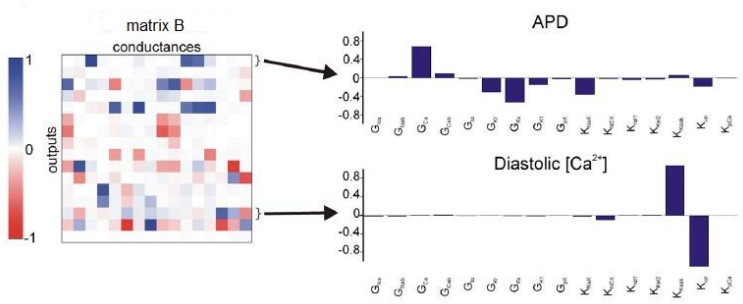

Figure 3.4: Example of regression matrix B, where each row represents the contributions of the conductances to a particular output. The bar graphs corresponding to the two outputs APD and diastolic $[Ca^{2+}]$.

As described above, the input and output matrices are mean-centered and normalized by their standard deviations, which are computed for each column. Thus each element of **B** is defined relative to the relevant standard deviations. It is also important to note that conductances (Gs), changes in time constants (ps), and the two outputs are log-transformed prior to performing the regression. Thus, an increase by one standard deviation represents a 20% increase in the parameter. Shifts in the voltage dependence of activation or inactivation (Vs) can be either positive or negative and are therefore not log-transformed before regression. For these parameters one standard deviation represents a shift of 2 mV.
All simulations were performed using software written in the scientific computing language Matlab (The Mathworks, Natick, MA).

3.3 Rate-dependence

After results of multivariable regression, I studied the rate-dependence. Simulations were performed with 100 stimuli to achieve steady state and the duration of the last AP was collected for regression analysis. As the standard deviation of the log-trasformed APDs was different at two BCLs, respectively 0.154 and 0.122 for APD and $\Delta[Ca^{2+}]_i$, the regression coefficients corresponding to fast rate were scaled by the factor 0.122/0.154 for display. This scaling ensures that the two bar graphs are equivalent in terms the percentage change in APD caused by a given increase or decrease in an ionic conductance. Same for $\Delta[Ca^{2+}]_i$ scaled by the factor 0.594/0.488.
To compare parameters variation at slower rate and faster rate, I plotted the results in the same figure. An example is shown in Fig.3.5.

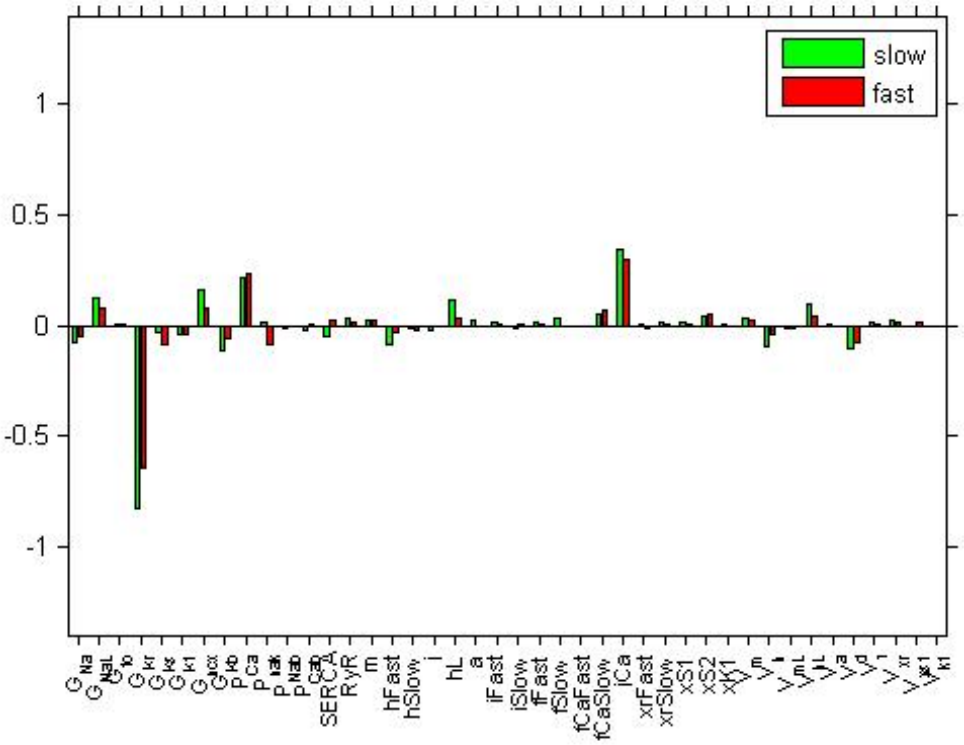

Figure 3.5: Example of regression coefficients at slow and fast rate.

To fully understand the rate-dependence, a matrix **B** was calculated as the difference between slow and fast rate by the subtraction:

$$B = |B_{slow}| - |B_{fast}|$$

where B_{slow} is the B_{PLS} matrix at slow rate and B_{fast} is the B_{PLS} matrix at fast rate. Every row of matrix **B** represents the contribution of each parameter to a particular output. Positive values indicate a RRD of parameters in relation to the respective output, negative values indicate a FRD. In fact, RRD occurs when I have a bigger effect of parameter at slow rate than at fast rate, whereas FRD occurs when there is a bigger effect of parameter at fast rate than at slow rate. An example is shown in figure Fig.3.6.

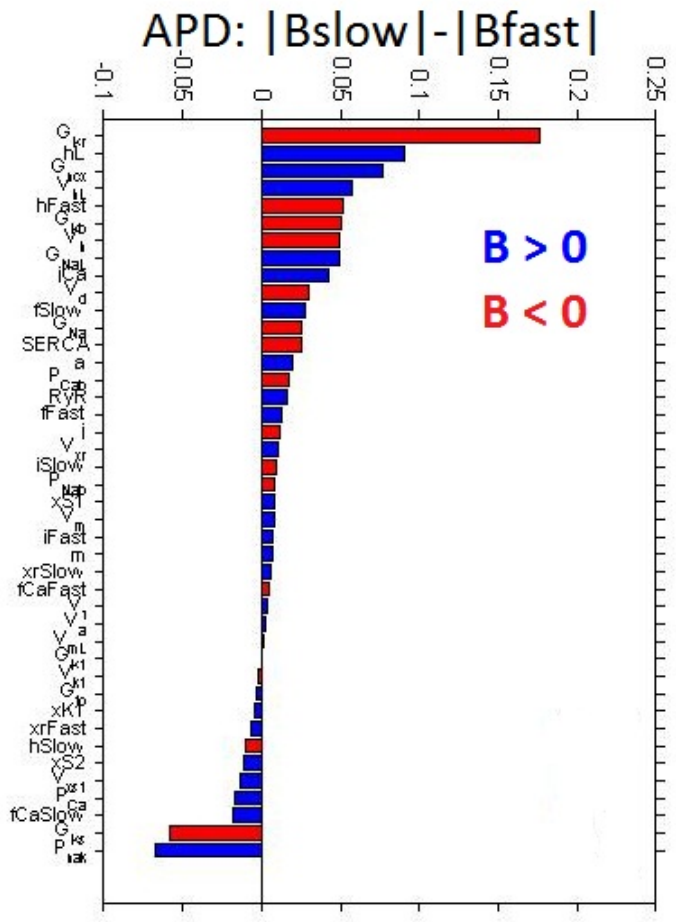

Figure 3.6: Example of rate-dependence of regression coefficients respect to a single output. Each bar is the result of $|B_{slow}| - |B_{fast}|$ and represents the contributions of each parameter to the output. Positive values indicate a RRD of parameters in relation to the respective output, negative values indicate a FRD.

3.4 Test of the rate-dependence

The second stage of the computational experiment aimed to understand if the prediction of rate-dependence was correct and to determine why partic-

ular perturbations might be RRD or FRD in terms of ionic currents changes. Two conductances were studied: the conductance of rapid delayed rectifier K^+ current (**Gkr**) for the RRD and the conductance of Na^+/K^+ ATPase current for the FRD (**Pnak**). The choice of these two was because they were the ones which varied more. Simulations were performed with a train of 100 stimuli delivered at two BCL: 5000 ms and 500 ms. The response to the last stimulus in the series was saved. G_{kr} was changed by a logarithmic scale factor from 0 to 0.25 by a step of 0.05, while P_{nak} was changed by a logarithmic scale factor from 0 to 3 with a step of 0.25.

3.4.1 A new method: matrix $\Delta\Delta Q$

To fully understand the perturbation effect to the other currents, these currents were integrated with the "trapezoid rule" to calculate total "fluxes" through each pathway. A new matrix **Q** was created where each column represents an integrated current. Simulations were performed at slow and fast rate and matrices Q_{slow} and Q_{fast} were created. In Fig.3.7 each current is plotted at fast rate (dotted line) and at slow rate (solid line) during parameter variation (i.e. G_{Kr}).

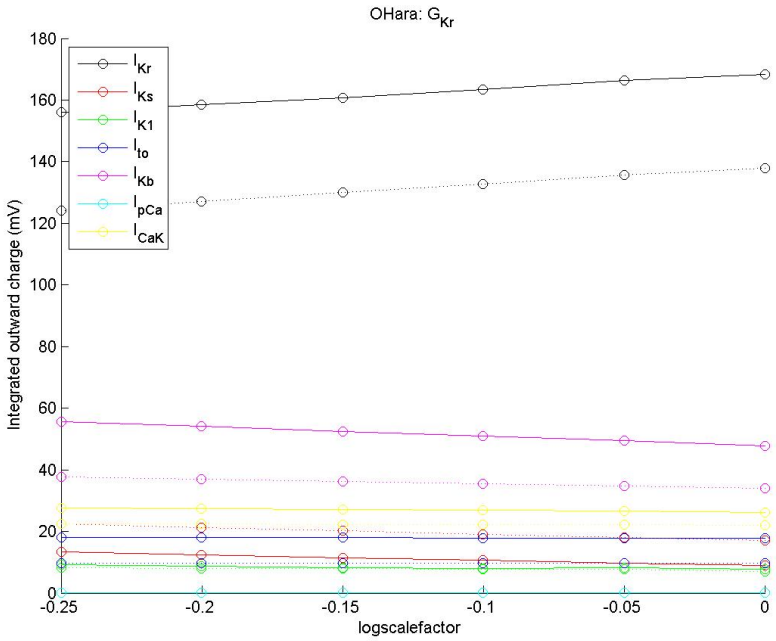

Figure 3.7: Example of integrated outward currents changed after perturbation of G_{kr}. Dotted lines represent each column of matrix Q_{fast} at fast rate, whereas solid line represent each column of matrix Q_{slow} at slow rate.

To investigate more these results, an additional matrix $\Delta\Delta Q$ was calculated by the following equation:

$$\Delta\Delta Q = ((Q_{perturbation,fast} - Q_{control,fast}) - (Q_{perturbation,slow} - Q_{control,slow})) =$$

$$= (\Delta Q_{fast} - \Delta Q_{slow}) \tag{3.1}$$

where $Q_{perturbation}$ is the **Q** matrix calculated with the maximum variation of parameter G and $Q_{control}$ is the **Q** matrix calculated without the variation of the parameter.

Fig. 3.8 explains the equation 3.1 for the single current I_{Kr}. At first, maximum perturbation value at fast rate (**Fmax**) was subtracted from the control value (**Fctrl**) to create the ΔQ_{fast} matrix; then maximum perturbation

value at slow rate (**Smax**) was subtracted from the control value (**Sctrl**) to create the ΔQ_{slow} matrix. Matrix $\Delta\Delta Q$ was created by the equation $\Delta Q_{fast} - \Delta Q_{slow}$.

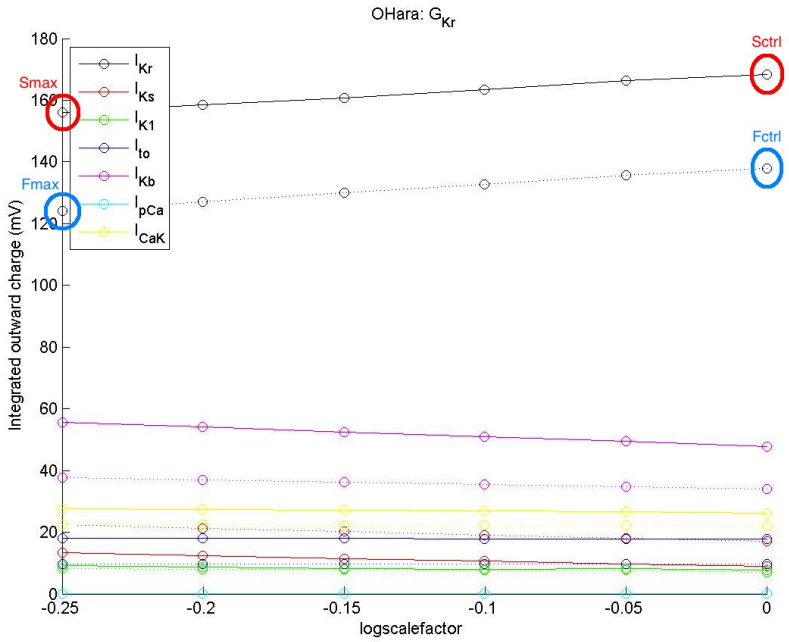

Figure 3.8: Example of calculation of $\Delta\Delta Q$ matrix. Matrix ΔQ_{fast} is the result of $F_{ctrl} - F_{max}$, where F_{ctrl} is the integrated current value in control and F_{max} is the integrated current value at maximum "logscalefactor" value; matrix ΔQ_{slow} is the result of $S_{ctrl} - S_{max}$, where S_{ctrl} is the integrated current value in control, whereas S_{max} is the integrated current value at maximum "logscalefactor" value. Matrix $\Delta\Delta Q$ is created by the equation $\Delta Q_{fast} - \Delta Q_{slow}$.

Subsequently, each column of matrix $\Delta\Delta Q$ was plotted in a bar graph. An example is shown in Fig.3.9, obtained for G_{kr}.

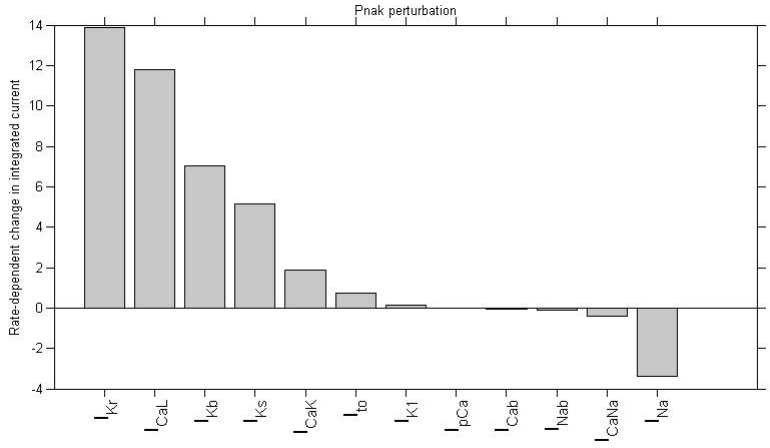

Figure 3.9: Matrix $\Delta\Delta Q$ computed by equation 3.1 after G_{kr} perturbation. Positive value contributes to RRD, negative value contributes to FRD.

Equation 3.1 (and consequently Fig. 3.9) is a good method to explain the influence of perturbation to the other currents and, in particular, the rate-dependence of each one. The rules are the following:

- a positive value of $\Delta\Delta Q$ contributes to reverse rate-dependence (RRD).
- a negative value of $\Delta\Delta Q$ contributes to forward rate-dependence (FRD).

Current contributions can be explaind by the following principles:

1. Perturbation induces a large current variation only at slow rate ($\Delta Q_{fast} < \Delta Q_{slow}$):

   $\Delta\Delta Q < 0 \Longrightarrow$ Less prolongation at slow, FRD.

2. Perturbation induces a large current variation only at fast rate ($\Delta Q_{fast} > \Delta Q_{slow}$):

   $\Delta\Delta Q > 0 \Longrightarrow$ Less prolongation at fast, RRD.

3. Effects of perturbation are identical at fast and slow rates ($\Delta Q_{fast} = \Delta Q_{slow}$):

   Equivalent AP prolongation, $\Delta\Delta Q = 0$.

3.4.2 Perturbations effect

Next step was to clarify which was the effect of the disturbance to the other currents and if this influence could be forward rate-dependent, reverse rate-dependent or rate independent. To achieve this goal I followed two approaches:

(1) Simulations with different end-time of repolarization at both rates (Fig.3.10(a)).

(2) Simulations with same end-time of repolarization at fast and slow rate (Fig.3.10(b)).

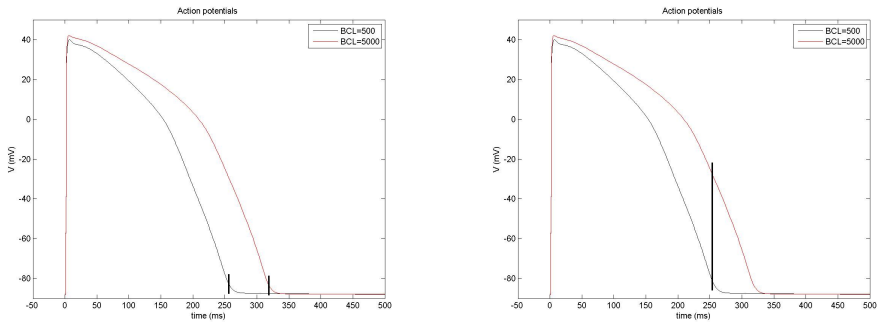

(a) Different end-time (b) Same end-time

Figure 3.10: Different end-times to study the influence of parameters perturbation. At same end-time (b), delayed rectifier currents should be smaller at slow rate than at fast rate. At different end-time (a), currents can be studied in all their behavior.

To implement these approaches, I run a first simulation with a logarithmic scale-factor varied from 0 to 1.4 by a step of 0.2 for both parameters. Because P_{nak} value, from rate-dependence result, was smaller than G_{kr} value (Fig.4.6), two new scale factors were obtained from this simulation: one for P_{nak} (1.4) and one for G_{kr} (0.1241). Using these new scale factors, I run a second simulation with the goal to obtain the results explained above:

1. AP shapes of two parameters compared to AP shape of control, at fast and slow rate;

2. change in integrated currents at fast and slow rate, to have a critical view of rate-dependence;

3. rate-dependence of integrated currents.

4. to plot the currents of grater interest and show the difference between fast and slow rate.

Results are shown in the following chapter.

Chapter 4

Results

4.1 Regression analysis results in the O'Hara model

Fig.4.1 shows sample action potential shapes and the calcium transient shapes obtained with randomly-varying parameters at fast rate with the O'Hara model. The plot is made of 300 APs and 300 Ca^{2+} transients. The figure shows the last AP and the last Ca^{2+} transient in sequence of 100 stimulated at 500 ms.

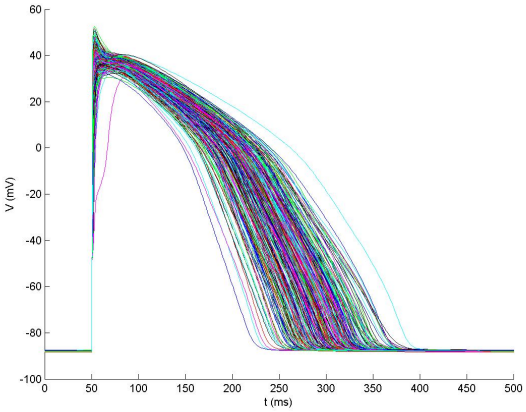

(a) Action potential

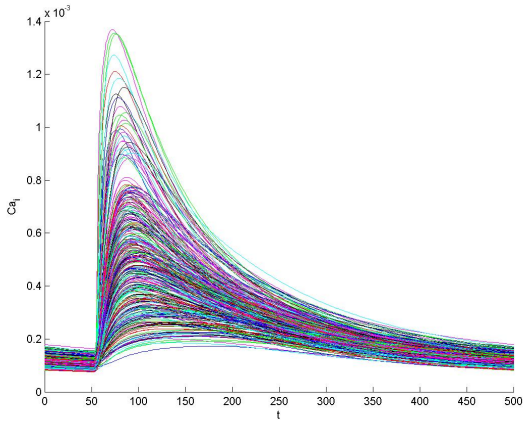

(b) Intracellular calcium

Figure 4.1: Action potentials (a) and calcium transients (b) in the O'Hara model. The plot is made of 300 APs and 300 Ca^{2+} transients.

Fig.4.2 and Fig.4.3 illustrate how parameter changes in affect outputs steady-state. Bar graphs represent parameter sensitivities for selected outputs. Each bar is a row of the regression matrix B_{PLS} and constitutes the contribution of each of the parameters to a particular output. At the beginning four outputs were studied: from top to bottom, respectively, APD, Vrest, Vpeak and calcium transient.

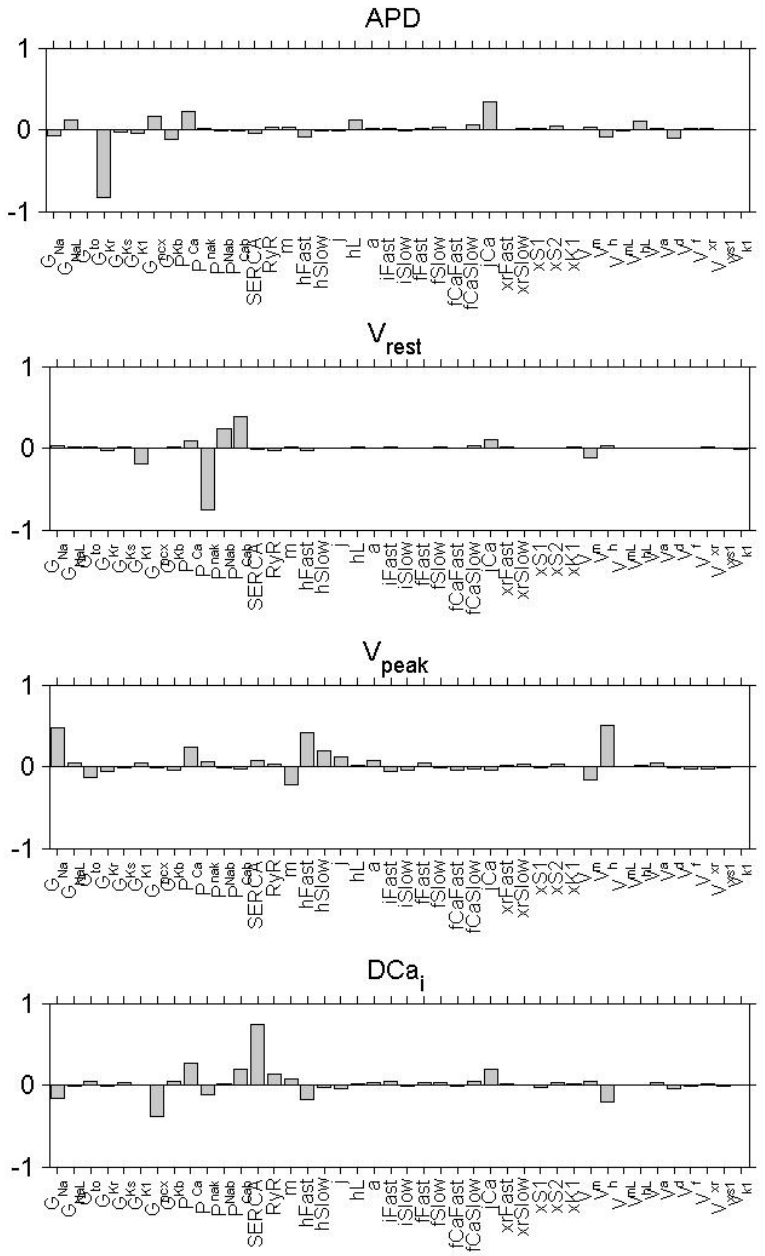

Figure 4.2: Results of the regression analysis at slow rate. The graph indicates how changes in parameters affect four outputs (2 Hz pacing) at slow rate. Regression performed with 300 simples. The parameters controlling variability (σ) were set to 0.1823 for conductances and p variables, 2 mV for voltage shift variables.

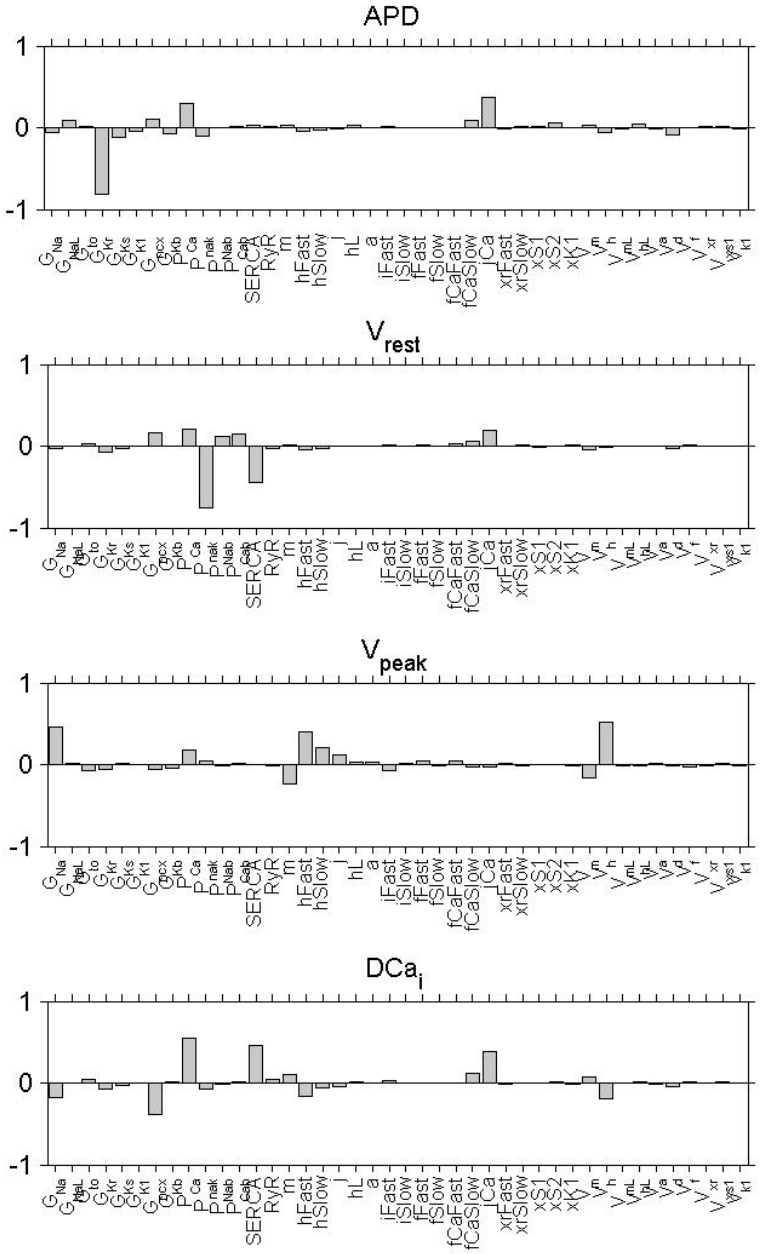

Figure 4.3: Results of the regression analysis at fast rate. The graph indicates how changes in parameters affect four outputs (2 Hz pacing) at fast rate. Regression performed with 300 trials. The parameters controlling variability (σ) were set to 0.1823 for conductances and p variables, 2 mV for voltage shift variables.

Fig.4.4 demonstrates the accuracy of regression analysis method at fast and slow rates for the O'Hara model. For the four outputs, scatter plots show the "actual" values, generated by randomizing the baseline parameters in the model, versus the "predicted" values, calculated with the regression model. The large values of R^2 (> 0.9) indicate that the prediction of the regression method are quite accurate.

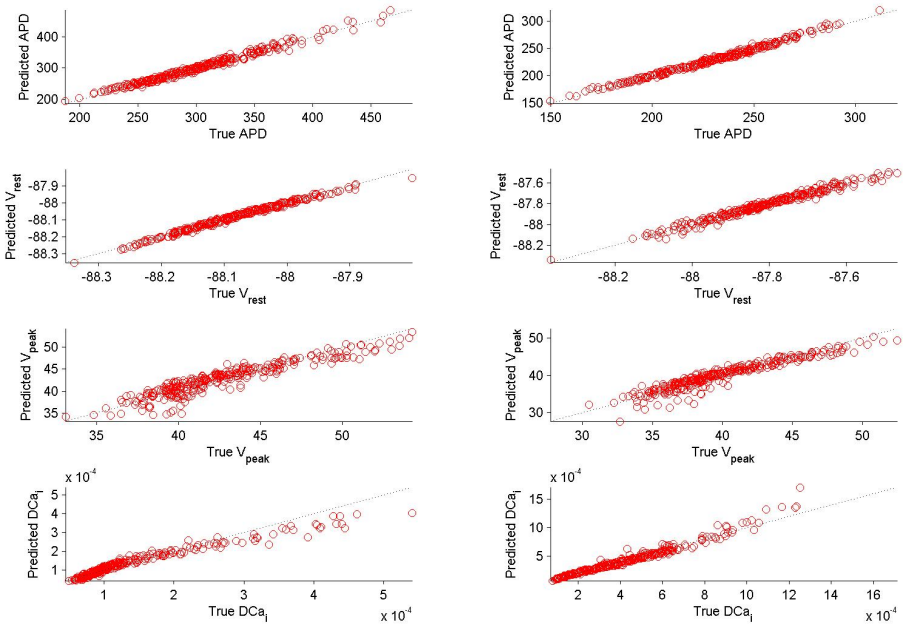

(a) Prediction at slow rate (b) Prediction at fast rate

Figure 4.4: Scatter plots show the $R^2 > 0.9$ of the regression analysis predictions for four outputs in the O'Hara model at slow (a) and fast (b) rate. The empirical regression model generates accurate predictions, even when non-linear parameters are included in the analysis. $R^2 = 0.9934$ for APD, $R^2 = 0.9894$ for $\Delta[Ca^{2+}]_i$.

4.2 Rate-dependence results in the O'Hara model

Fig.4.5 shows parameters variation obtained at slower and faster rate with the O'Hara model, respectively for APD and $\Delta[Ca^{2+}]_i$.

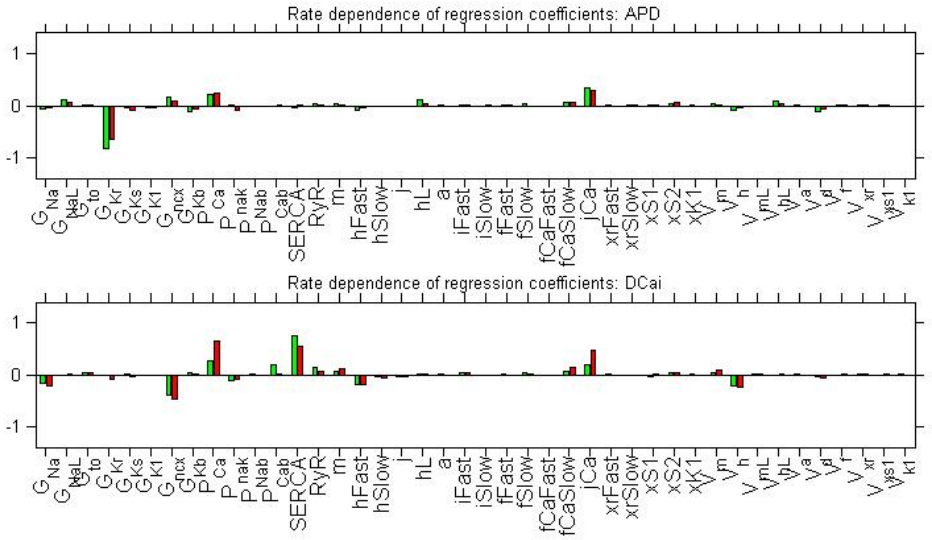

Figure 4.5: Regression coefficients obtained with the O'Hara model. The model cell was paced at two basic cycle length (BCL), 5000 ms and 500 ms. In both cases, parameters were randomized and 100 stimuli were applied to achieve steady state. Two outputs were studied: APD and $\Delta[Ca^{2+}]_i$. *Since the standard deviation of the log-trasformed APDs was different at BCL=5000ms (0.154) than at BCL=500ms (0.122),the regression coefficients corresponding to BCL=500ms were scaled by the factor* 0.122/0.154 *for display. This scaling ensures that the two bar graphs are equivalent in terms of percentage change in APD caused by a given increase or decrease in a ionic conductance.* $\Delta[Ca^{2+}]_i$, *instead, was scaled by the factor* 0.594/0.488.

From previous results, the difference between slow and fast rate was calculated by the subtraction $|Bslow| - |Bfast|$, where Bslow is the B_{PLS} matrix at slow rate and Bfast is the B_{PLS} matrix at fast rate. Results are displayed

in Fig.4.6 and Fig.4.7, respectively, for APD and calcium transient, where positive values represent RRD, whereas negative values represent FRD.

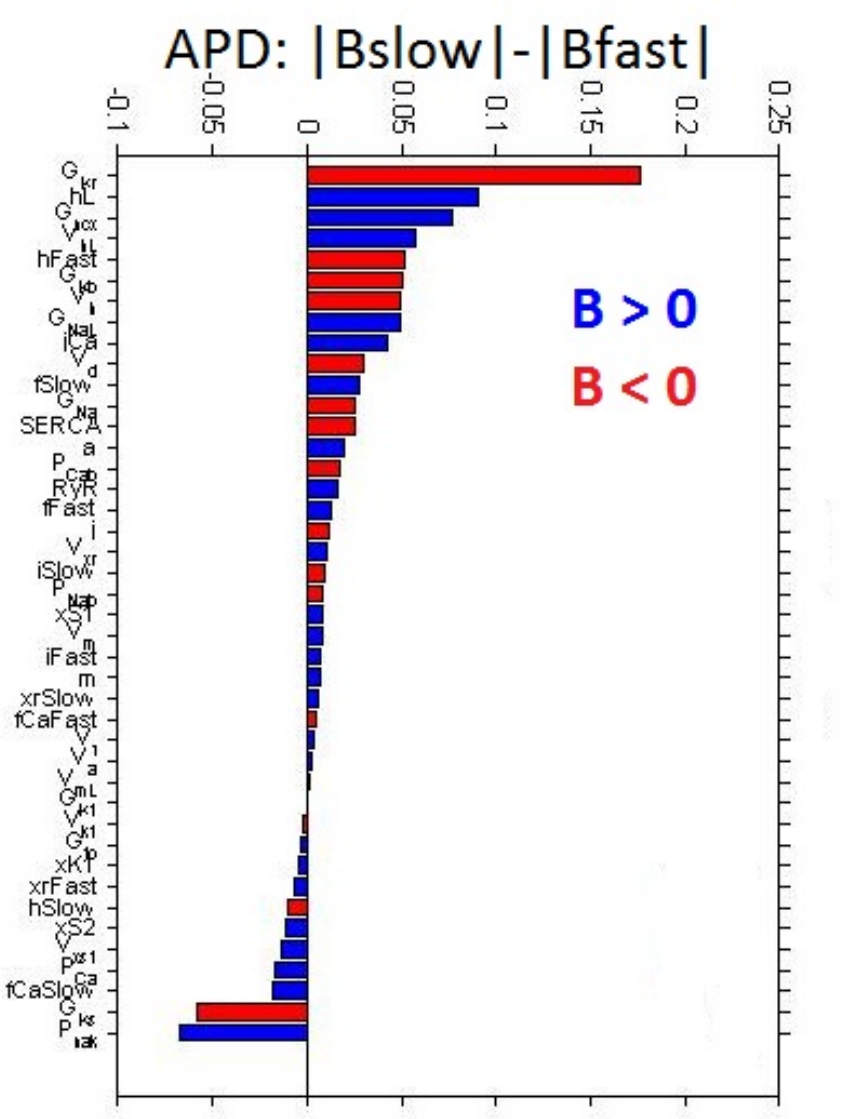

Figure 4.6: Rate-dependence of regression coefficients for APD. The graph shows the result of $|B_{slow}| - |B_{fast}|$. B is the regression matrix where each row represents the contributions of each of parameters to a particular output. Positive values represent a RRD, whereas negative values represent FRD.

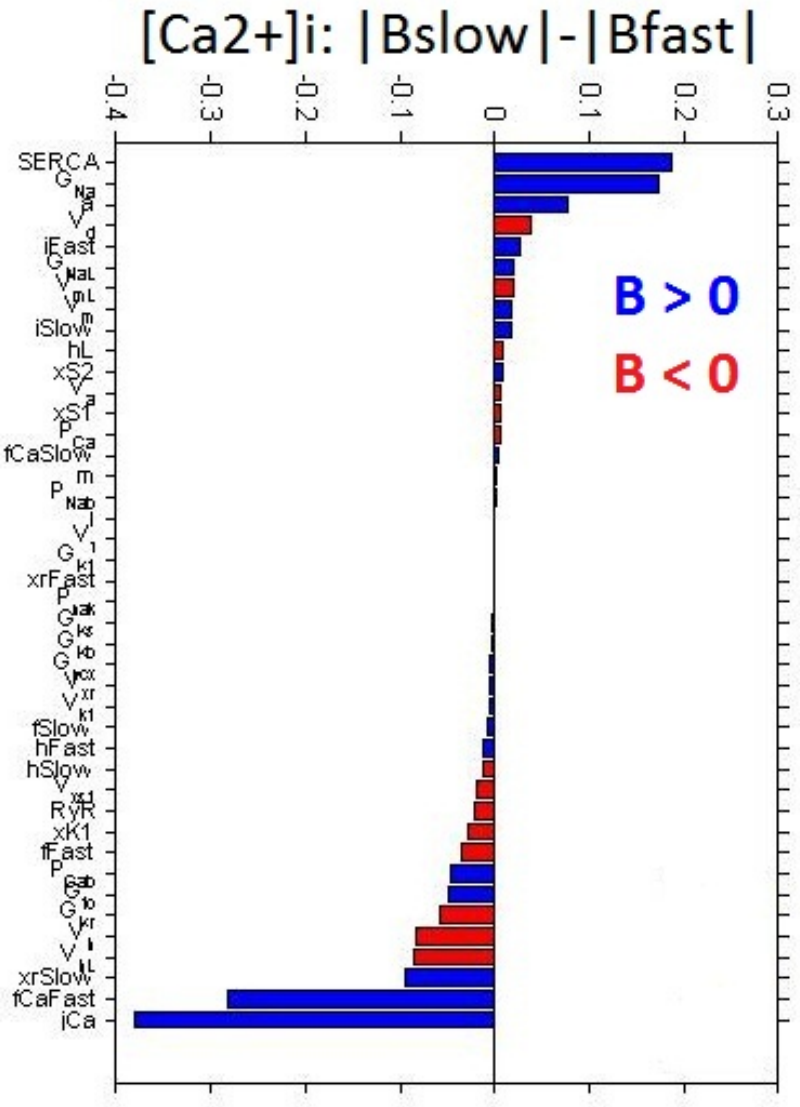

Figure 4.7: Rate-dependence of regression coefficients for $\Delta[Ca_i^{2+}]$. The graph shows the result of $|B_{slow}| - |B_{fast}|$. B is the regression matrix where each row represents the contributions of each of the parameters to a particular output. Positive values represent a RRD, whereas negative values represent FRD.

Figure 4.8 displays the distributions of APD and $\Delta[Ca^{2+}]_i$ during the

simulations. Short APs were randomly removed from the data set to keep the median APD and $\Delta[Ca^{2+}]_i$ roughly constant.

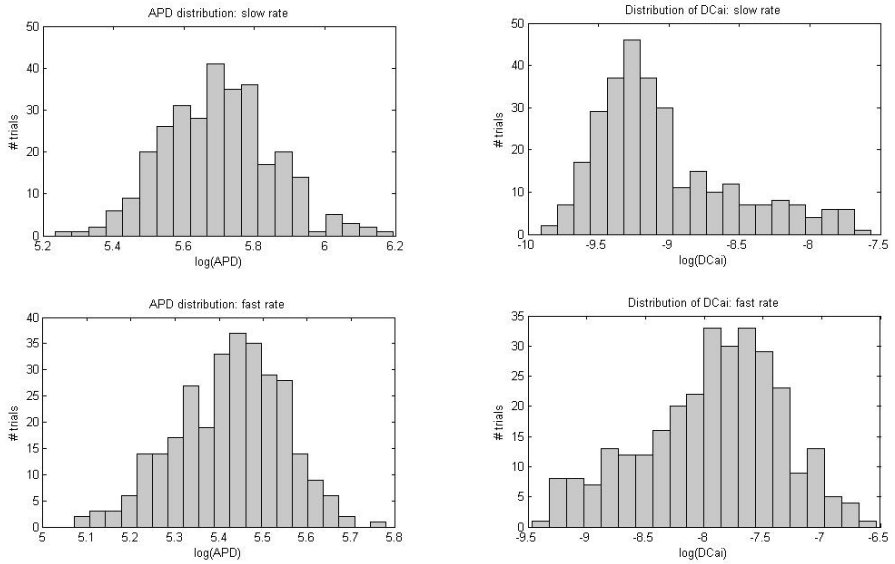

(a) APD (b) $\Delta \mathrm{Ca}_i^{2+}$

Figure 4.8: Distributions from a set of 300 trials of APD (a) and $\Delta[Ca^{2+}]_i$ (b) performed with the O'Hara model at slow rate (top graph) and at fast rate (bottom graph). Short APs were randomly removed from the data set to keep the median APD and $\Delta[Ca^{2+}]_i$ roughly constant.

As clinical evidence, in the last period, has suggested that anti-arrhythmic drugs which prolong the refractory period by means of prolongation of the cardiac action potential duration (APD) are beneficial in preventing the recurrence of clinically relevant human arrhythmias, I decided to study only APD as output of the model.
Fig.4.6 and 4.7 show that conductances which change more for the RRD are G_{kr} (the first one) and G_{ncx} (the third one), while the conductances which change more for the FRD are P_{nak} (the last one) and G_{Ks} (the second last). To fully understand how a perturbation can influence ionic currents and if this influence could be forward rate-dependent, reverse rate-dependent, or

rate-independent in the O'Hara model, I decided to perturb two parameters: G_{Kr} for the RRD and P_{nak} for the FRD. Results are shown in the following paragraphs.

4.2.1 Perturbation of G_{kr}

G_{kr} was perturbed by a scale factor e^x, where x is a vector varied from 0 to -0.25 by a step of 0.05. Fig.4.9 shows the last AP shape of each variation at slow rate (a) and fast rate (b).

To confirm regression model prediction (Fig.4.9) and rate-dependence result (Fig.4.6), Fig.4.10 illustrates the normalized change of APD after the variation of G_{kr}. This change has a bigger effect at slow rate (solid line) than at fast rate (dotted line).

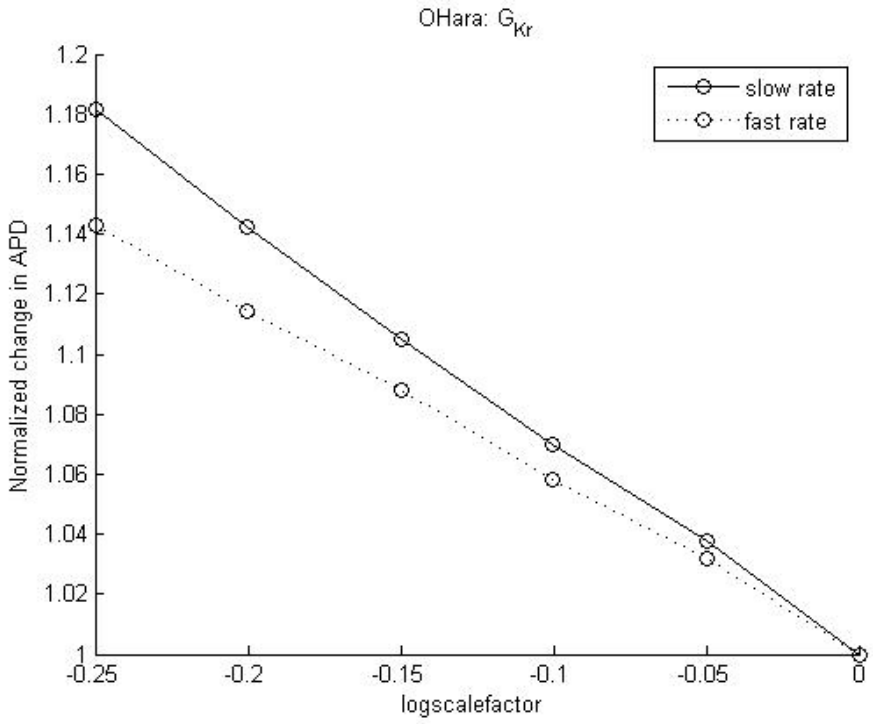

Figure 4.10: Effect of the variation of Gkr on APD normalized. This plot confirms the result of Fig.4.9. The change at slower rate (solid line) has a bigger effect than at faster rate (dotted line).

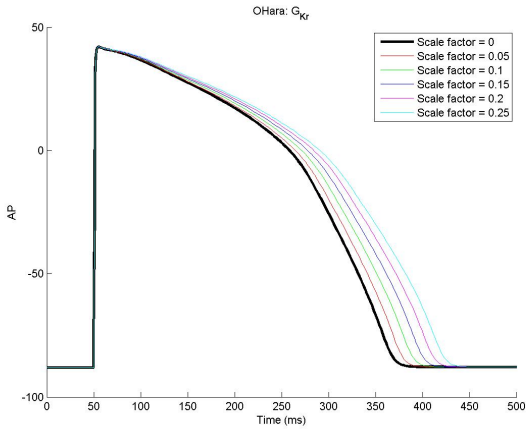

(a) Slow rate

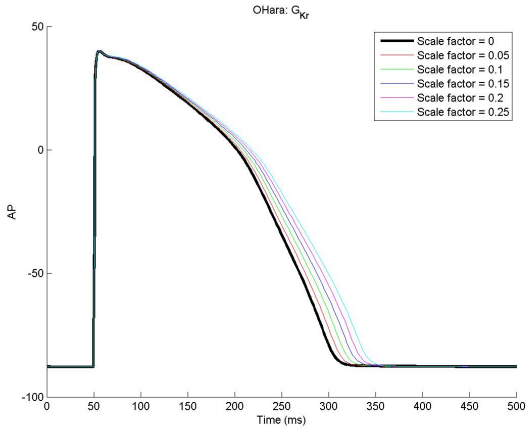

(b) Fast rate

Figure 4.9: Influence of Gkr after the variation of a scale factor e^x, where x is a vector varied from 0 to -0.25 by a step of 0.05. As Gkr is reverse rate-dependent, it has a smaller influence at faster rate (b) than at slower rate (a).

To understand which was the perturbation effect to the other currents, I applied a new method to display the results. Initially, ionic currents were integrated with the *trapezoid rule* to obtain the quantity of ionic charge through the respective conductance. Then, these "fluxes" were separated between inward and outward and two new matrices were calculated, Q_{inTot}

and Q_{outTot} respectively, where each column represents a "flux" through the respective conductance. Simulations were performed at slow and fast rate and matrices Q_{slow} and Q_{fast} were created. Fig.4.11 and Fig.4.12 show the integrated inward and outward currents during the variation of G_{kr} at fast rate (dotted line) and slow rate (solid line).

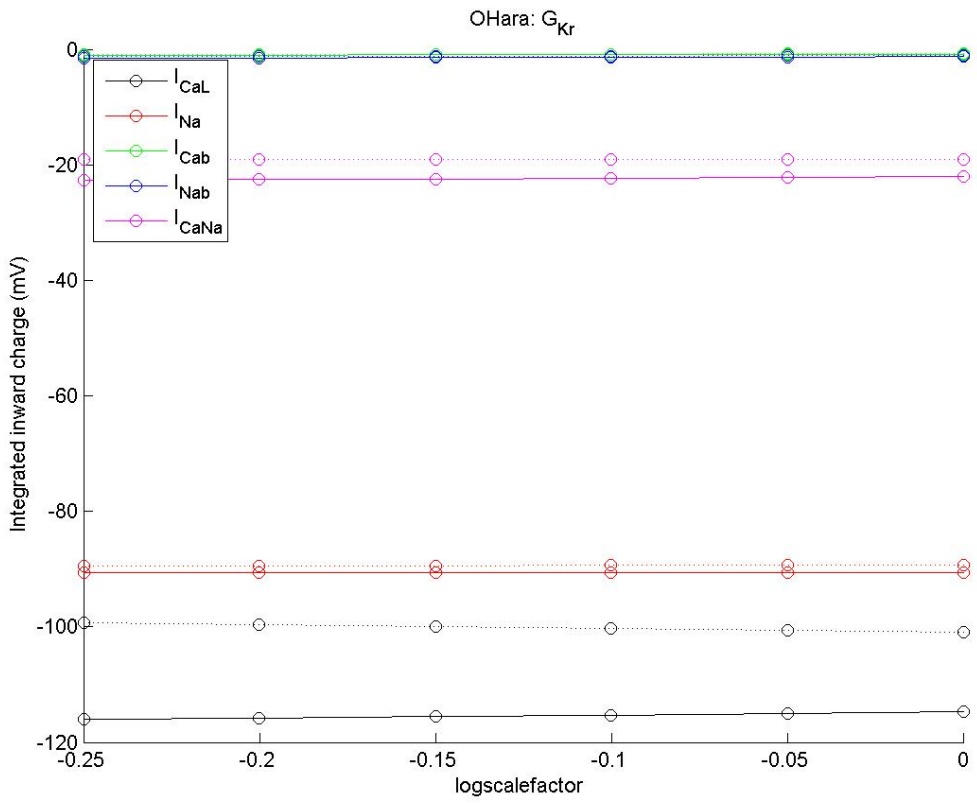

Figure 4.11: Integrated inward currents changed after perturbation of G_{kr}. Dotted lines represent each column of matrix Q_{fast} at fast rate, whereas solid line represent each column of matrix Q_{slow} at slow rate.

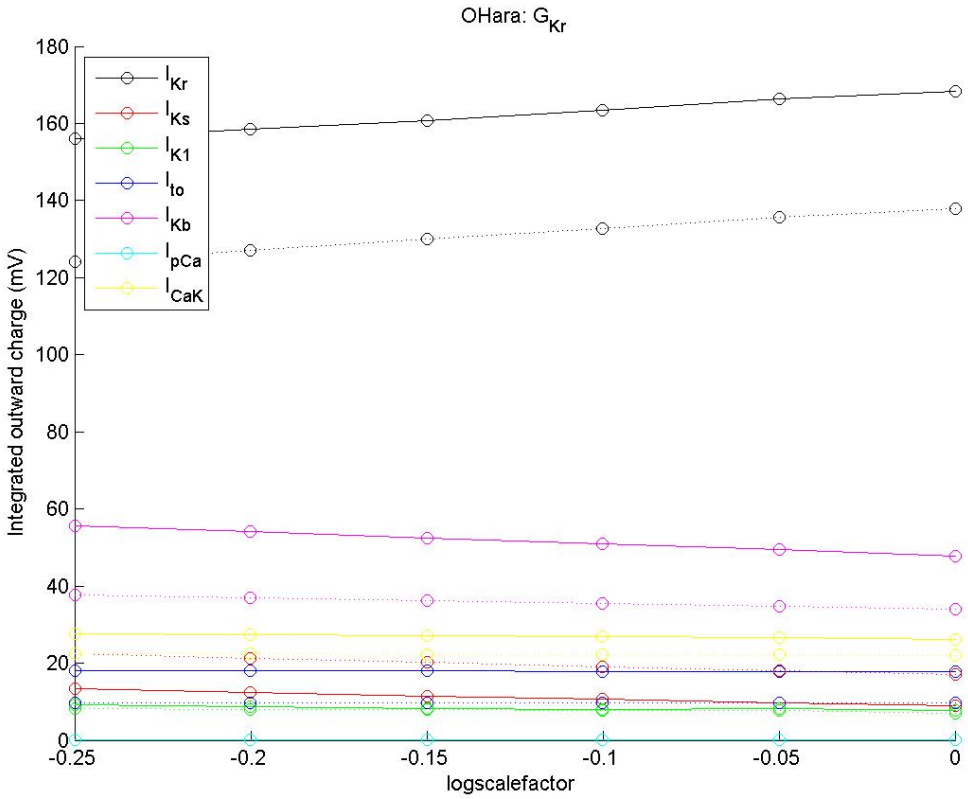

Figure 4.12: Integrated outward currents changed after perturbation of G_{kr}. Dotted lines represent each column of matrix Q_{fast} at fast rate, whereas solid line represent each column of matrix Q_{slow} at slow rate.

To investigate more on the difference between fast and slow rate, an additional matrix $\Delta\Delta Q$ was calculated by the equation 3.1. Fig.4.13 shows the influence of G_{kr} to the other currents, where each bar is a column of matrix $\Delta\Delta Q$. Positive values contributes to RRD, whereas negative values contributes to FRD.

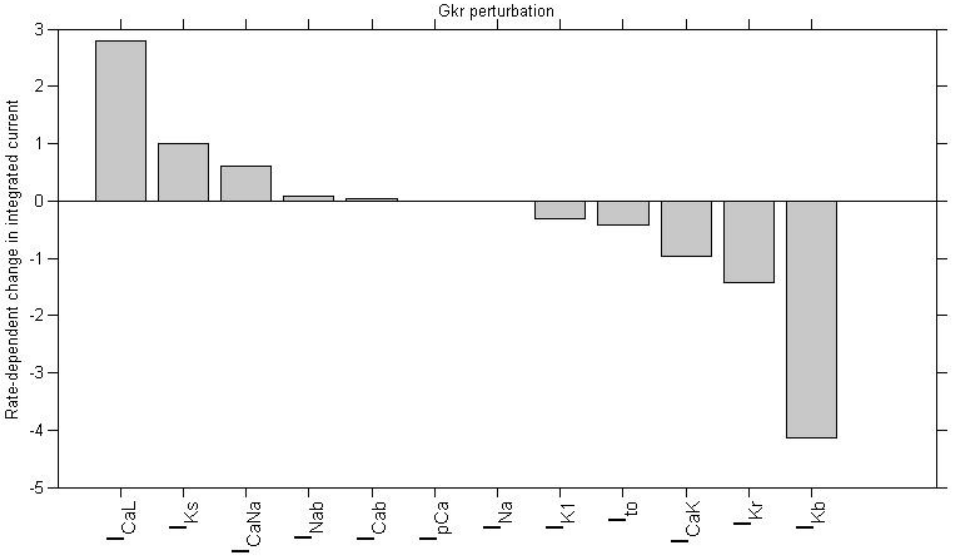

Figure 4.13: Rate-dependence of integrated currents after G_{kr} perturbation. Positive value contributes to RRD, negative value contributes to FRD. Larger values mean a greater influence of the parameter.

4.2.2 Perturbation of P_{nak}

P_{nak} was perturbed by a scale factor e^x, where x is a vector varied from 0 to -2 by a step of 0.25. Fig.4.14 shows the variations of AP shape during the perturbation at slow rate (a) and at fast rate (b).

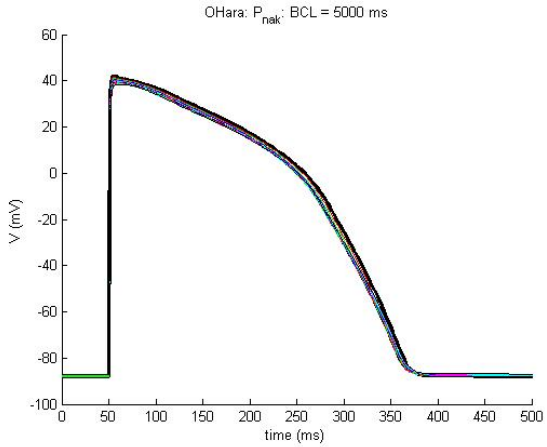

(a) Slow rate

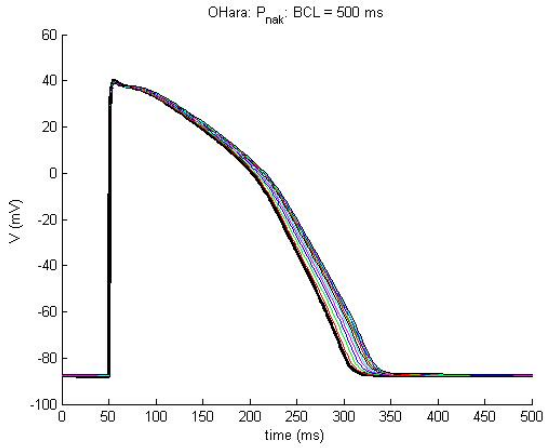

(b) Fast rate

Figure 4.14: Influence of Pnak after a variation of a scale factor of e^x where x is vector from 0 to -2 by a step of 0.25. As Pnak is forward rate-dependent, it has a smaller influence at fast rate (b) than at slow rate (a).

Fig.4.15 shows the FRD of P_{nak}. The effect at slow rate (solid line) is smaller than at fast rate (dotted line).

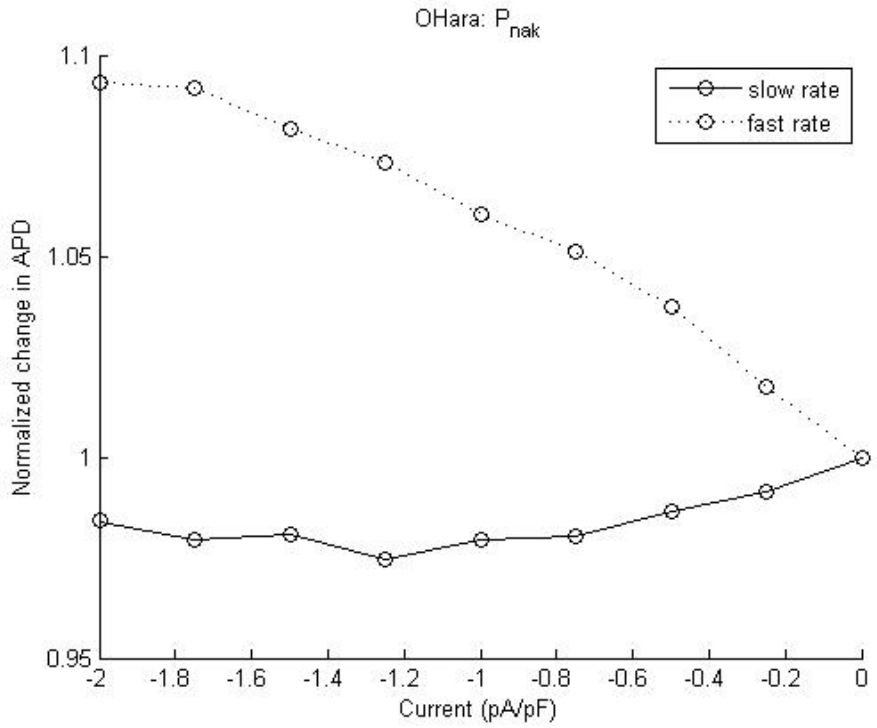

Figure 4.15: Effect of P_{nak} variations on APD normalized. The plot confirms the result of Fig. 4.14. The change at slow rate (solid line) has a smaller effect than at fast rate (dotted line).

Fig.4.16 shows the result for the inward currents, whereas Fig.4.17 shows the result for the outward currents. Each current is plotted at fast rate (dotted line) and at slow rate (solid line).

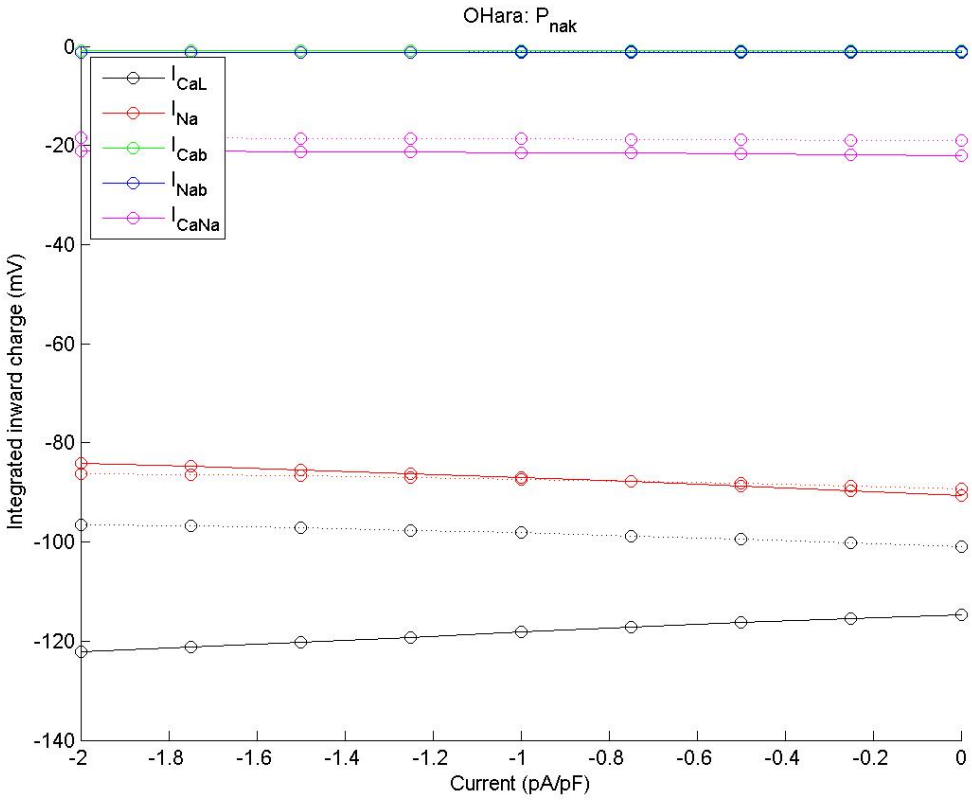

Figure 4.16: Integrated inward currents changed after perturbation of P_{nak}. Dotted lines represent each column of matrix Q_{fast} at fast rate, whereas solid line represent each column of matrix Q_{slow} at slow rate.

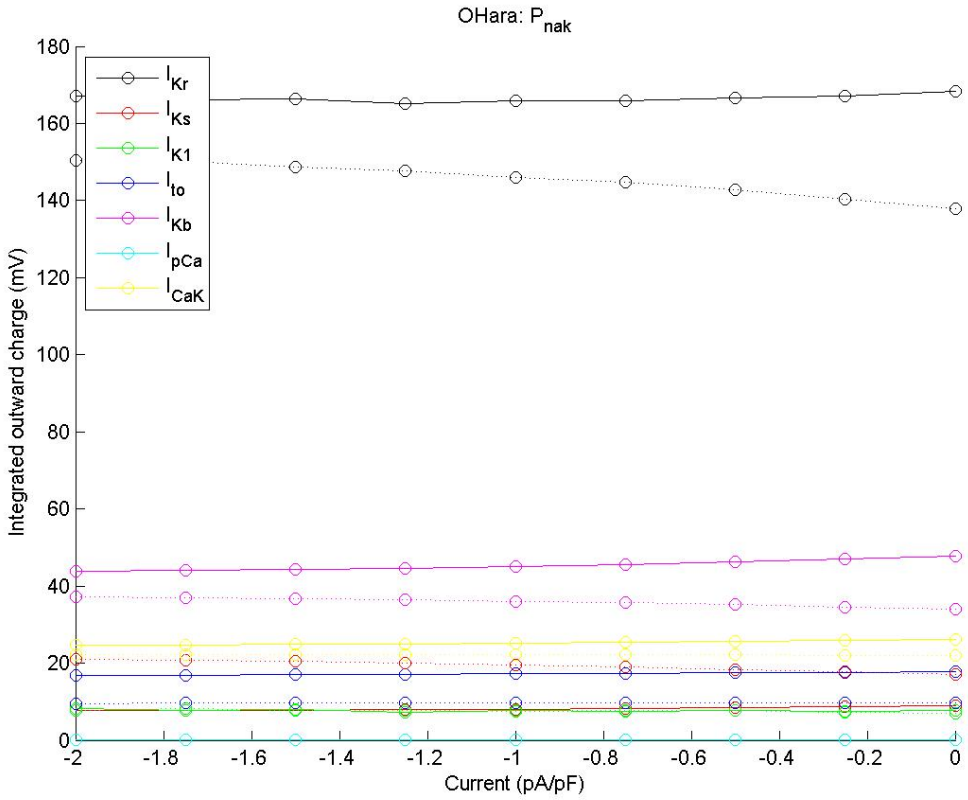

Figure 4.17: Integrated outward currents changed after perturbation of P_{nak}. Dotted lines represent each column of matrix Q_{fast} at fast rate, whereas solid line represent each column of matrix Q_{slow} at slow rate.

Fig.4.18 shows the result of matrix $\Delta\Delta Q$ for P_{nak}.

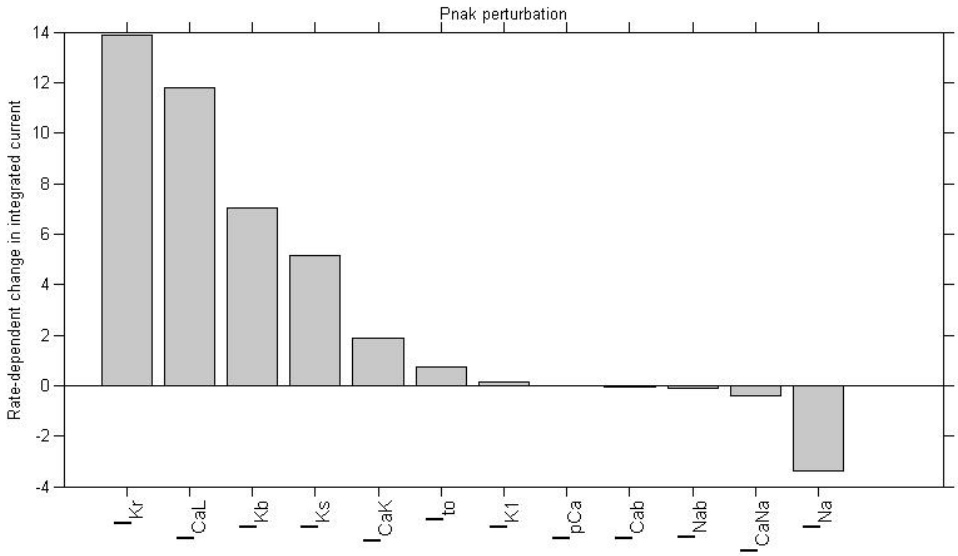

Figure 4.18: Rate-dependence of integrated currents after P_{nak} perturbation. Positive value contributes to RRD, negative value contributes to FRD.

4.3 Perturbations effect to the other currents

To clarify the effect of the disturbance to the other currents and to investigate if this influence could be forward rate-dependent, reverse rate-dependent or rate-independent, two approaches were followed:

1. Simulations with different end-time of repolarization at both rates (Fig.3.10(a)).

2. Simulations with same end-time of repolarization at fast and slow rate (Fig.3.10(b)).

4.3.1 Results with different end-time of repolarization

Fig.4.19 shows the last AP shapes computed with different end-time of repolarization in control (black line), after maximum P_{nak} variation (green

line) and after maximum G_{kr} variation (red line) at both rates. The figure shows a significant change in P_{nak} from slow to fast rate, whereas no significant change due to G_{kr}.

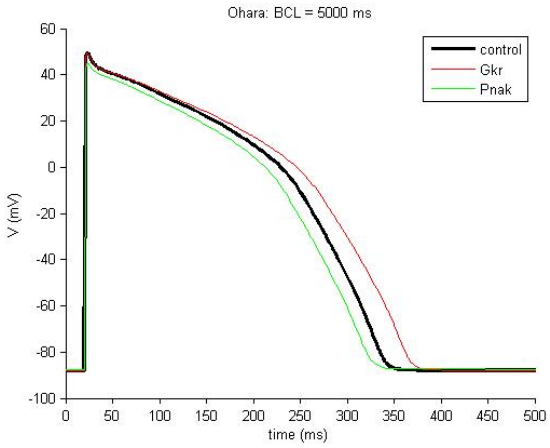

(a) Slow rate

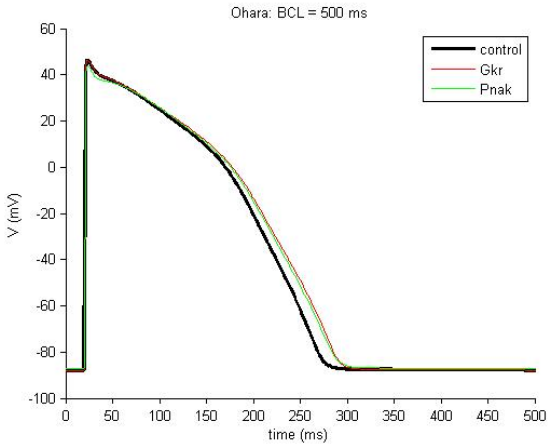

(b) Fast rate

Figure 4.19: AP shapes computed with different end-time of repolarization at slow (a) and fast (b) rate. There is a significant change in P_{nak} from slow to fast rate, whereas no significant change due to G_{kr}.

Fig.4.20 shows the rate-dependence of integrated currents using a different end-time of repolarization. Each bar is a column of $\Delta\Delta Q$ matrix calculated by equation 3.1 for G_{kr} (blue) and P_{nak} (red). It is evident that perturbation

of P_{nak} has a grater effect than G_{kr}.

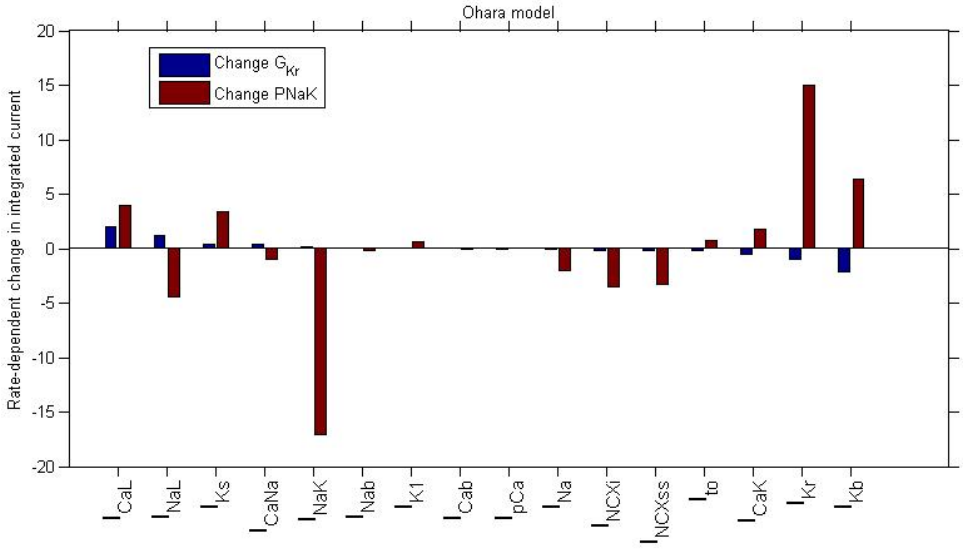

Figure 4.20: Rate-dependence of integrated currents at different end-time of repolarization. At different end-time, the AP is totally finished even at slow rate and the sum of forward and reverse currents must be equal to zero (equilibrium at steady-state). P_{nak} induces an evident forward rate-dependence to I_{NaK} current that is mostly compensated by I_{Kr} current, whereas I_{NaL}, forward rate-dependent current, is compensated by I_{Kb}.

Fig.4.21 shows the rate-dependence at slow (top) and fast (bottom) rate. These plots explain better what happens in Fig.4.20. For instance, I_{Kr} after P_{nak} variations has a different behavior at two rates: at fast rate is forward rate-dependent, whereas at slow rate is reverse rate-dependent; however, both behaviors lead to a RRD as shown in figure 4.20.

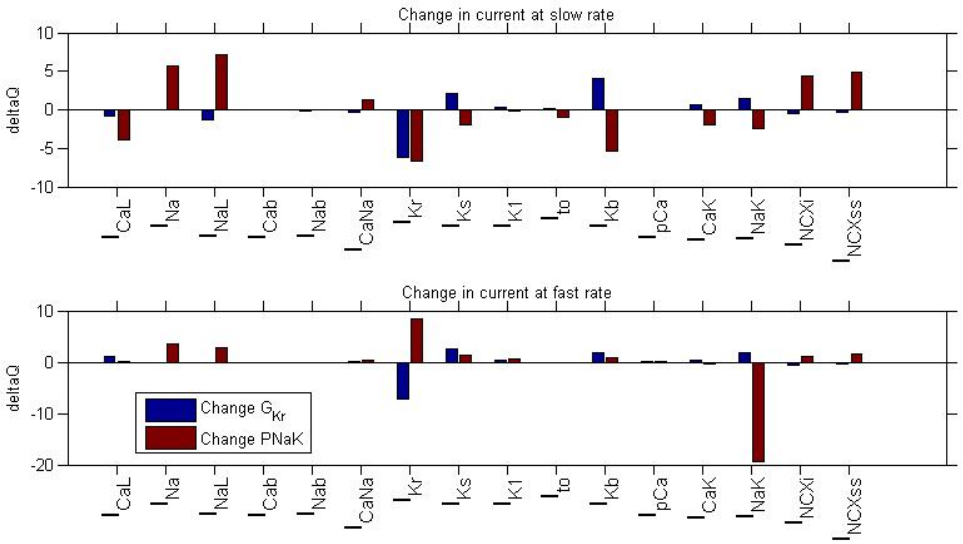

Figure 4.21: Change in currents with different end-time of repolarization at slow (top) and fast (bottom) rate. This plot explain more what happens in Fig.4.20.

Fig.4.22 shows what practically happens to the ionic currents calculated in the previous figures. Here, ionic currents are presented in control (black line), after maximum G_{kr} perturbation (red) and after maximum P_{nak} perturbation (blue).

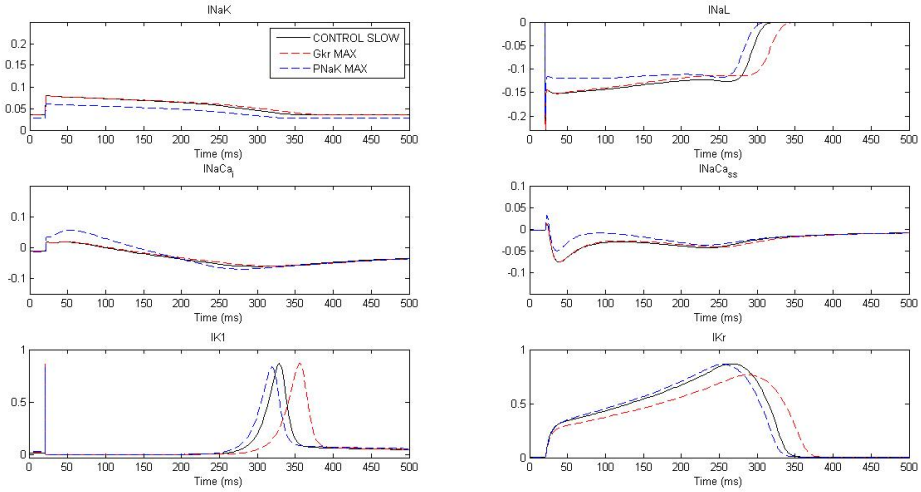

(a) Slow rate

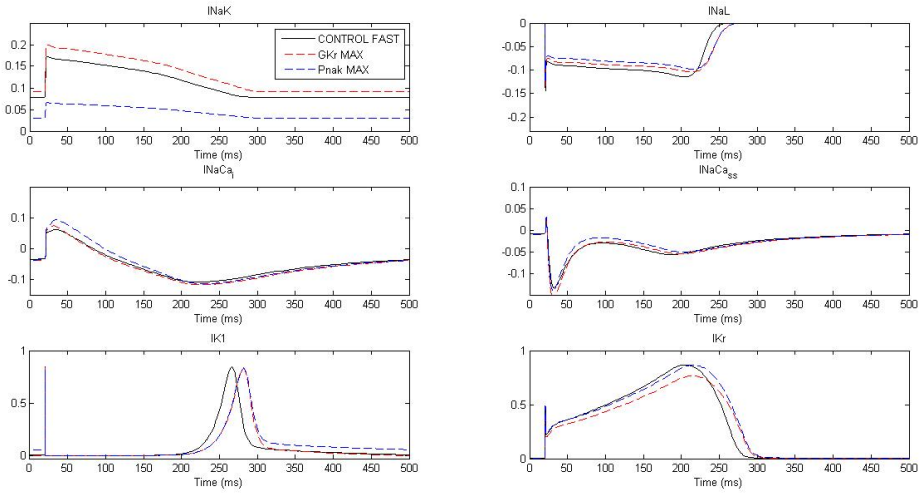

(b) Fast rate

Figure 4.22: Differences in currents at slow (a) and fast (b) rate with different end-time of repolarization. Black line is the current of control, red line is after maximum G_{kr} variation and blue line is after maximum P_{nak} variation.

4.3.2 Results with same end-time of repolarization

The same procedure was performed using the same repolarization end-time.

Fig.4.23 illustrates the last AP shapes in control (black line), after maximum P_{nak} variation (green line) and after maximum G_{kr} variation (red line) at both rates. Shapes are practically equal to the different repolarization end-time shapes.

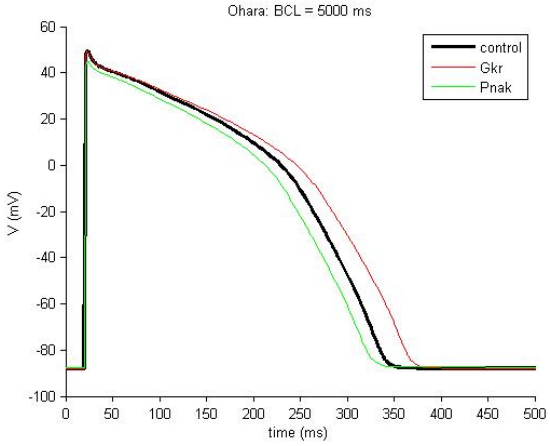

(a) Slow rate

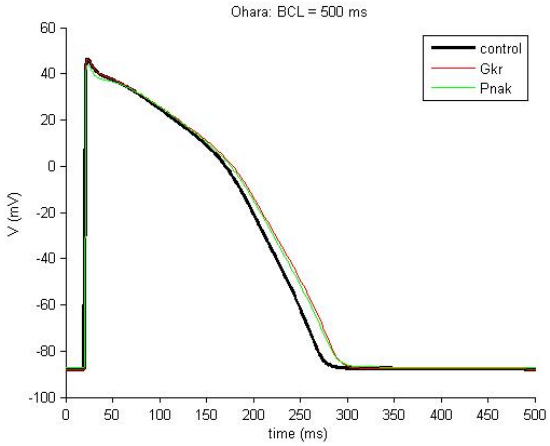

(b) Fast rate

Figure 4.23: AP shapes computed with same end-time of repolarization at slow (a) and fast (b) rate.

Fig.4.24 shows the rate-dependence of integrated currents. Each bar is a column of $\Delta\Delta Q$ matrix calculated by equation 3.1 for G_{kr} (blue) and P_{nak} (red). Here I can not have a balance of all currents, because the AP is not completely finished.

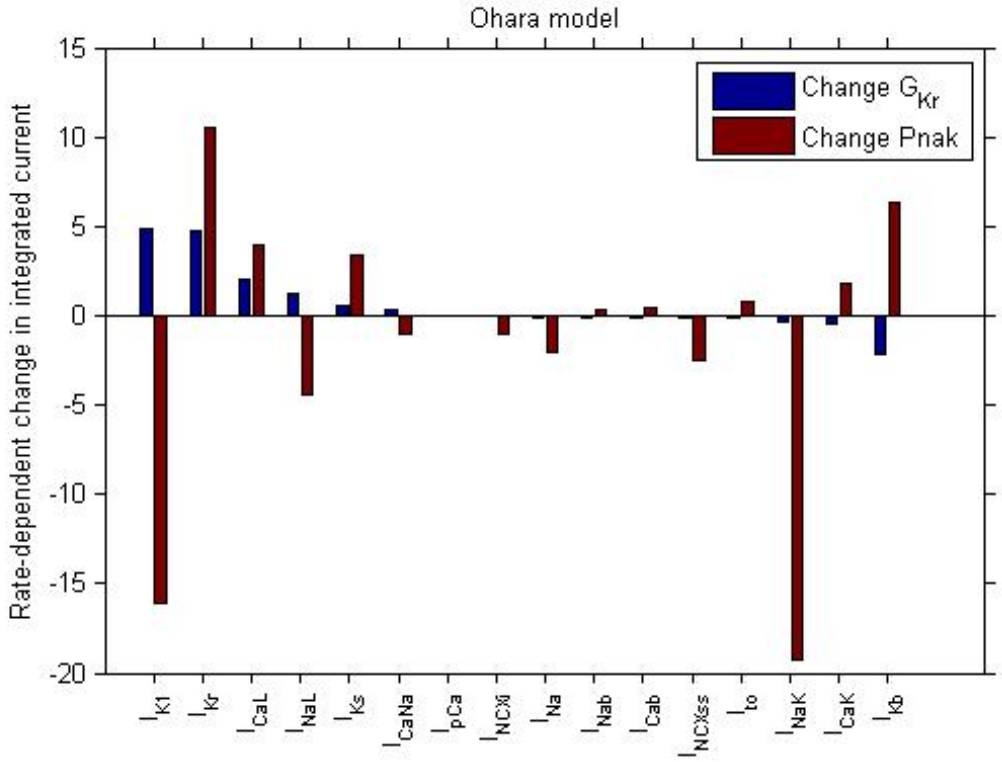

Figure 4.24: Rate-dependence of integrated currents with same end-time of repolarization. P_{nak} (red bars) induces a specific forward rate-dependence to I_{NaK} and I_{K1} currents which is partially compensated by the revers rate-dependent I_{Kr} and I_{Kb} currents. G_{Kr} (blue bars) induces a substantial reverse rate-dependence that is marked in I_{K1}, I_{Kr} and I_{CaL} currents.

Fig.4.25 shows the rate-dependence at slow (top) and fast (bottom) rate. These plots explain better what happens in Fig.4.24.

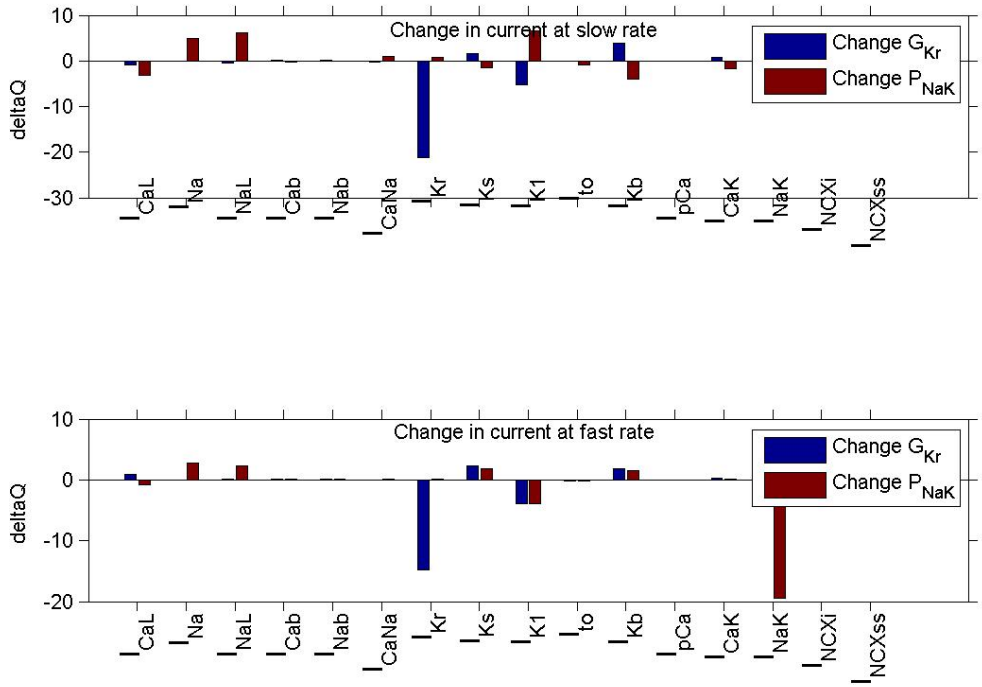

Figure 4.25: Change in current at slow (top) and fast (bottom) rates with same end-time of repolarization. Looking at both graphs, I_{Kr}, I_{K1} and I_{NaK} are the currents that change more. The first two due to variations in G_{Kr}, the other one due to variations in P_{nak}.

Fig.4.26 shows what practically happens to the ionic currents calculated in the previous figures. Here, ionic currents are presented in control (black line), after maximum G_{kr} perturbation (red) and after maximum P_{nak} perturbation (blue).

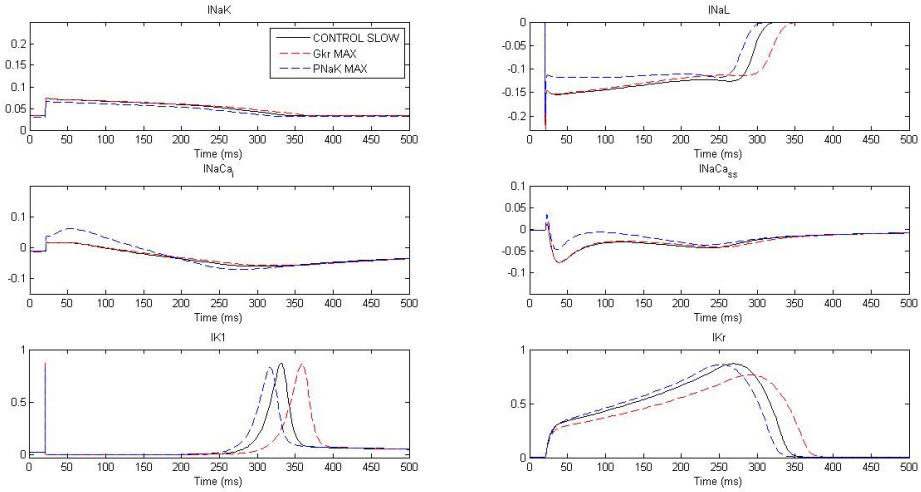

(a) Slow rate

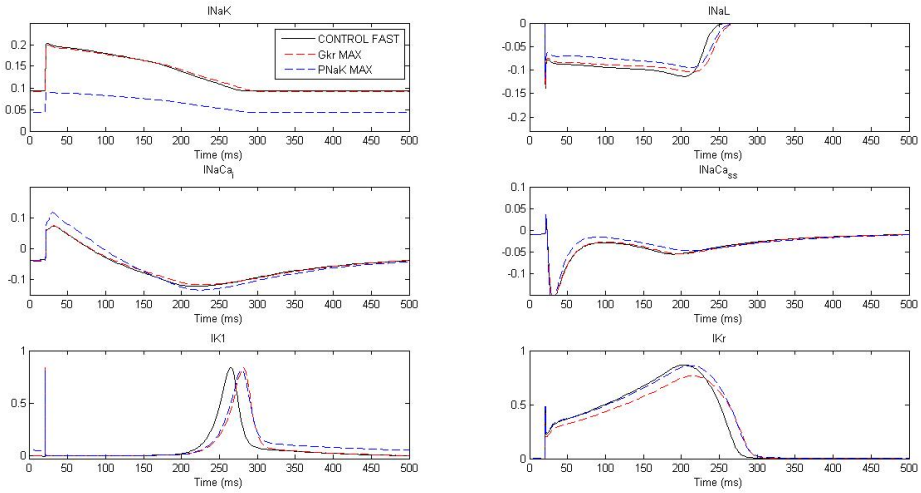

(b) Fast rate

Figure 4.26: Differences in currents at slow (a) and fast (b) rate with same end-time of repolarization.

4.4 Zaza's hypothesis

Initially, a first simulation was run with an arbitrary constant current varied from 0 to 0.5 pA/pF by a step of 0.1. The influence in the AP shape is shown in Fig.4.27.

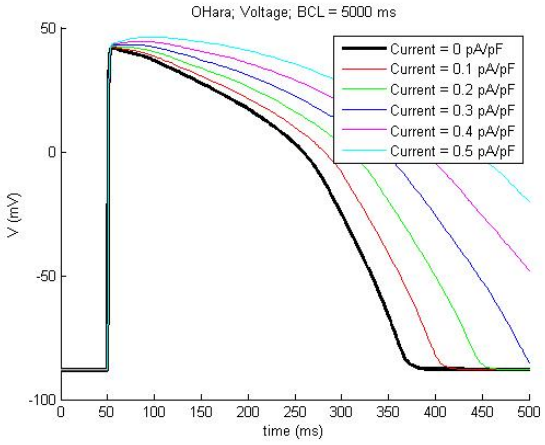

(a) Slow rate

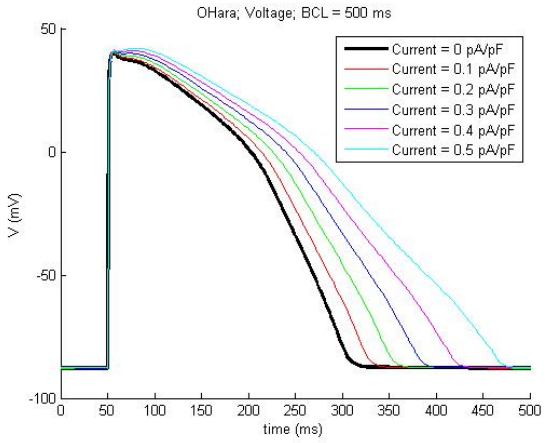

(b) Fast rate

Figure 4.27: Current injected influence after variations from 0 to 0.5 pA/pF at slow rate (a) and fast rate (b).

The effect of injected current at fast and slow rates is shown in Fig. 4.28.

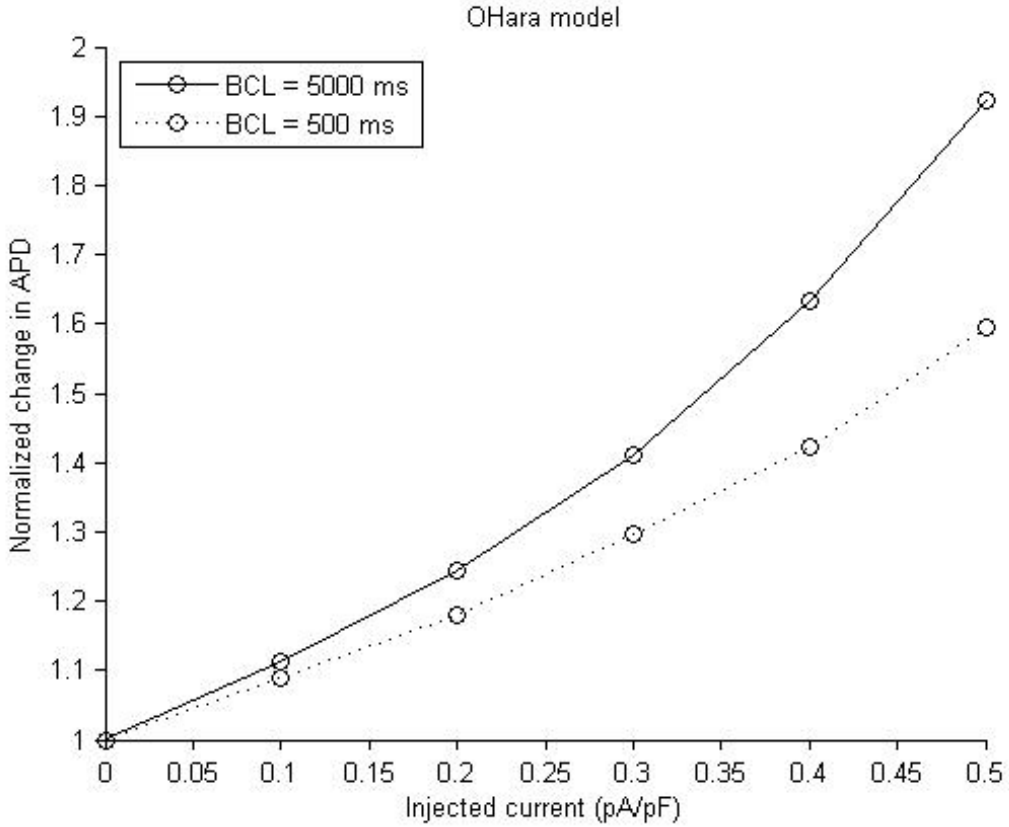

Figure 4.28: Current injection effect on APD normalized at first simulation. Plot confirms that at slow rate has a smaller effect than at fast rate (dotted line).

Integrated currents were also calculated in this simulation and results are shown in Fig. 4.29 and Fig. 4.30.

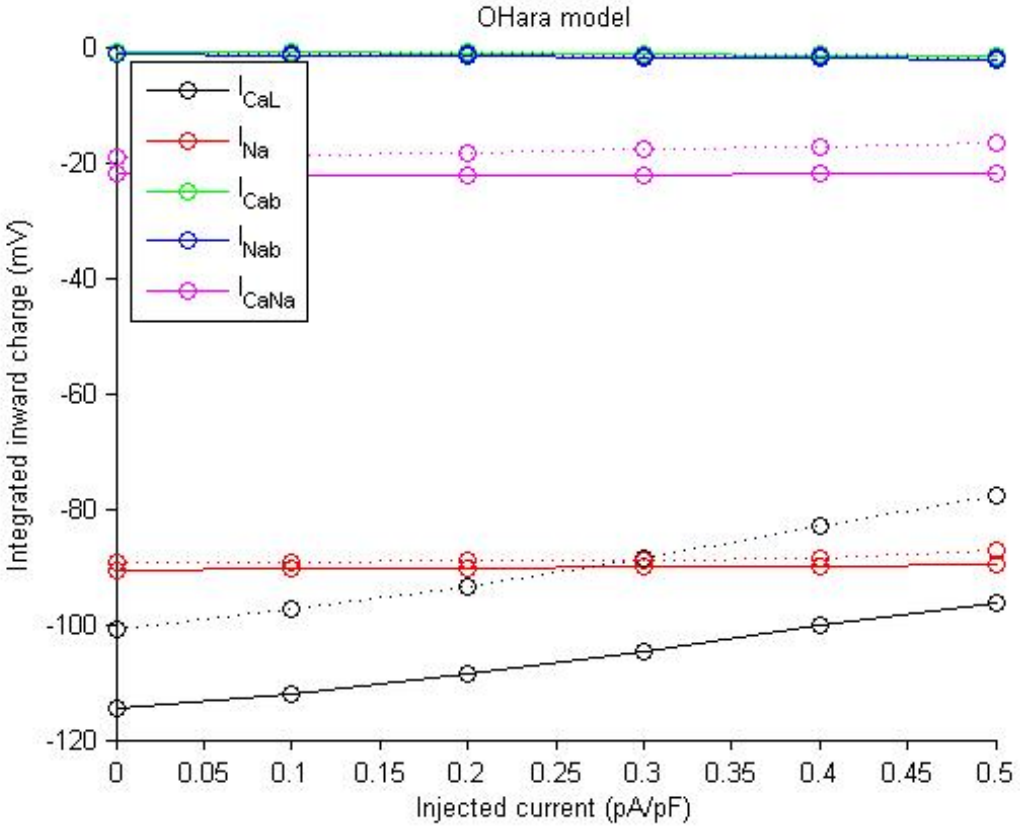

Figure 4.29: Integrated inward currents changed by current injected at first simulation. Dotted lines represent each column of matrix Q_{fast} at fast rate, whereas solid line represent each column of matrix Q_{slow} at slow rate.

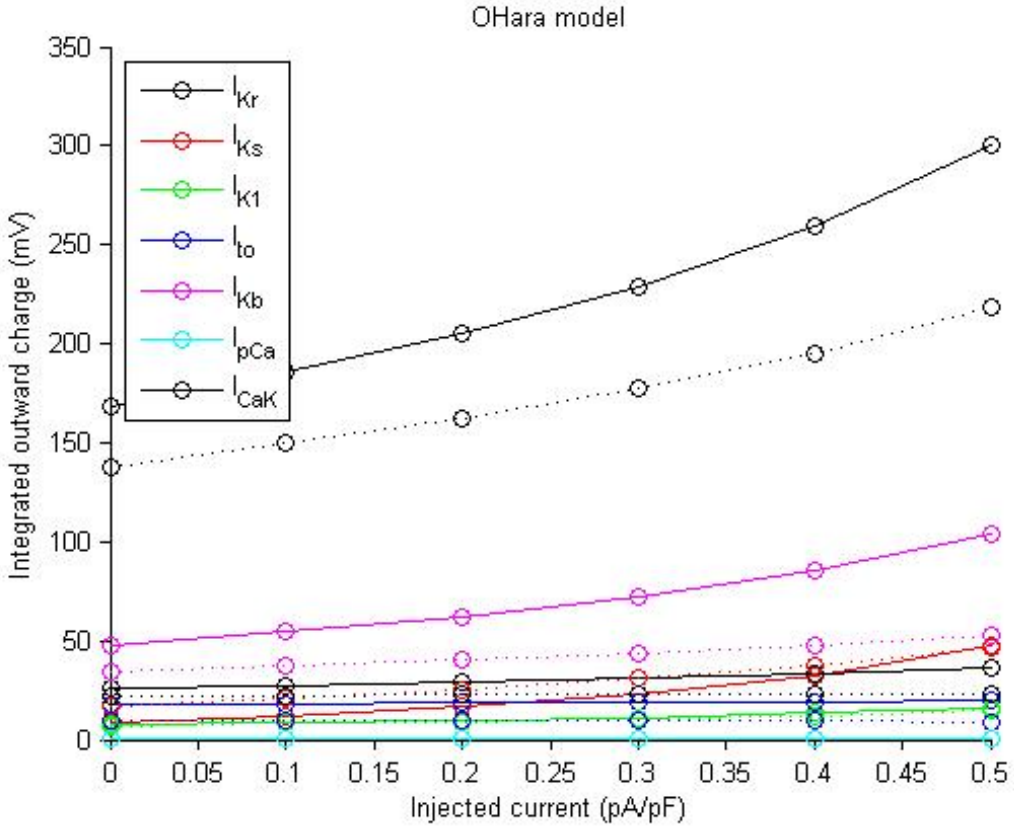

Figure 4.30: Integrated outward currents changed by current injected at first simulation. Dotted lines represent each column of matrix Q_{fast} at fast rate, whereas solid line represent each column of matrix Q_{slow} at slow rate.

Fig.4.31 shows the rate-dependence of integrated currents. Each bar is a column of $\Delta\Delta Q$ matrix calculated by equation 3.1.

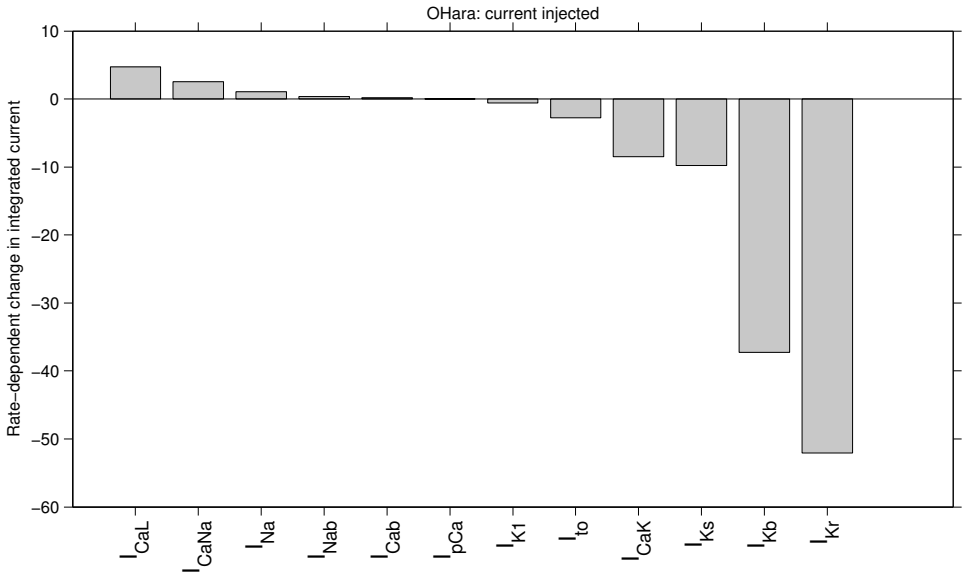

Figure 4.31: Rate-dependence of integrated currents influenced by current injected at first simulation.

Based on results such as shown in Fig.4.27, I reduced the current injected from 0 to 0.2 pA/pF by a step of 0.04, as shown in Fig.4.32.

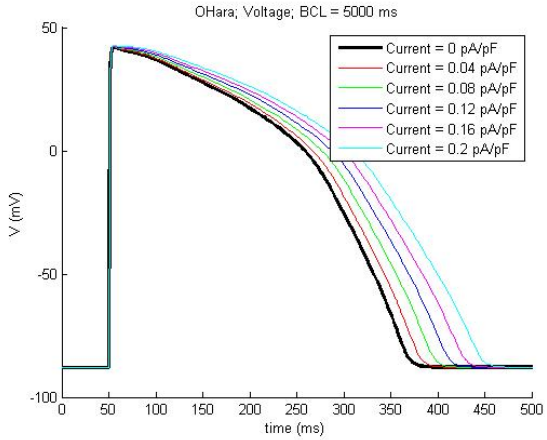

(a) Slow rate

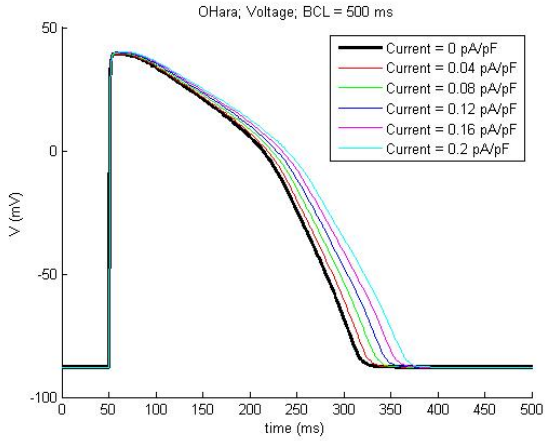

(b) Fast rate

Figure 4.32: Current injected influence after variations from 0 to 0.2 pA/pF at slow rate (a) and fast rate (b).

Fig.4.33 confirms a greater effect at slower rate than at faster rate.

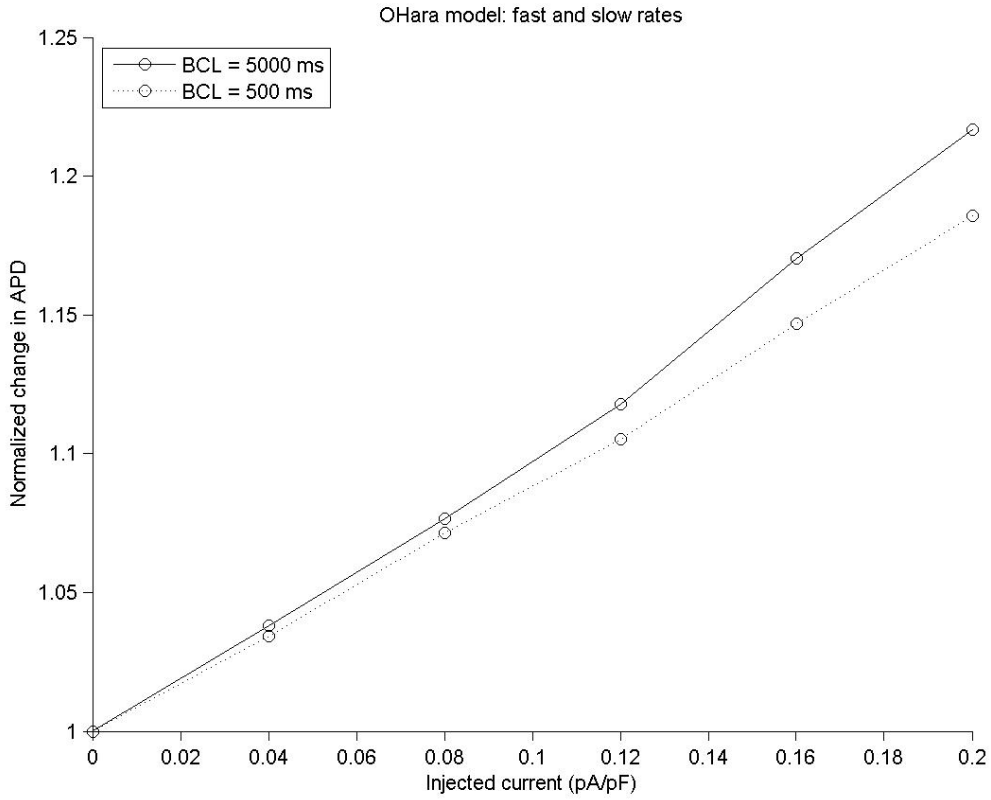

Figure 4.33: Effect of the current injection modified on APD normalized. Plot confirms that at slow rate has a smaller effect than at fast rate (dotted line).

After current injection modification integrated currents were calculated and the influence of the injected current is shown in Fig. 4.34 and Fig. 4.35.

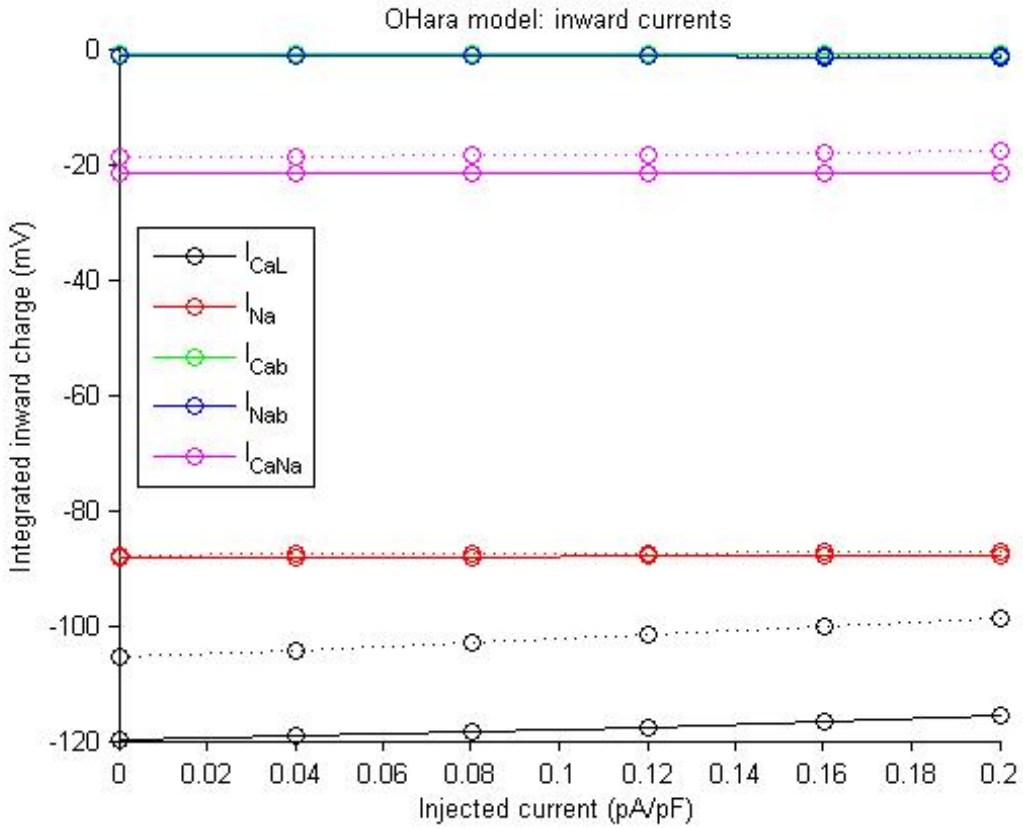

Figure 4.34: Integrated inward currents changed by current injected. Dotted lines represent each column of matrix Q_{fast} at fast rate, whereas solid line represent each column of matrix Q_{slow} at slow rate.

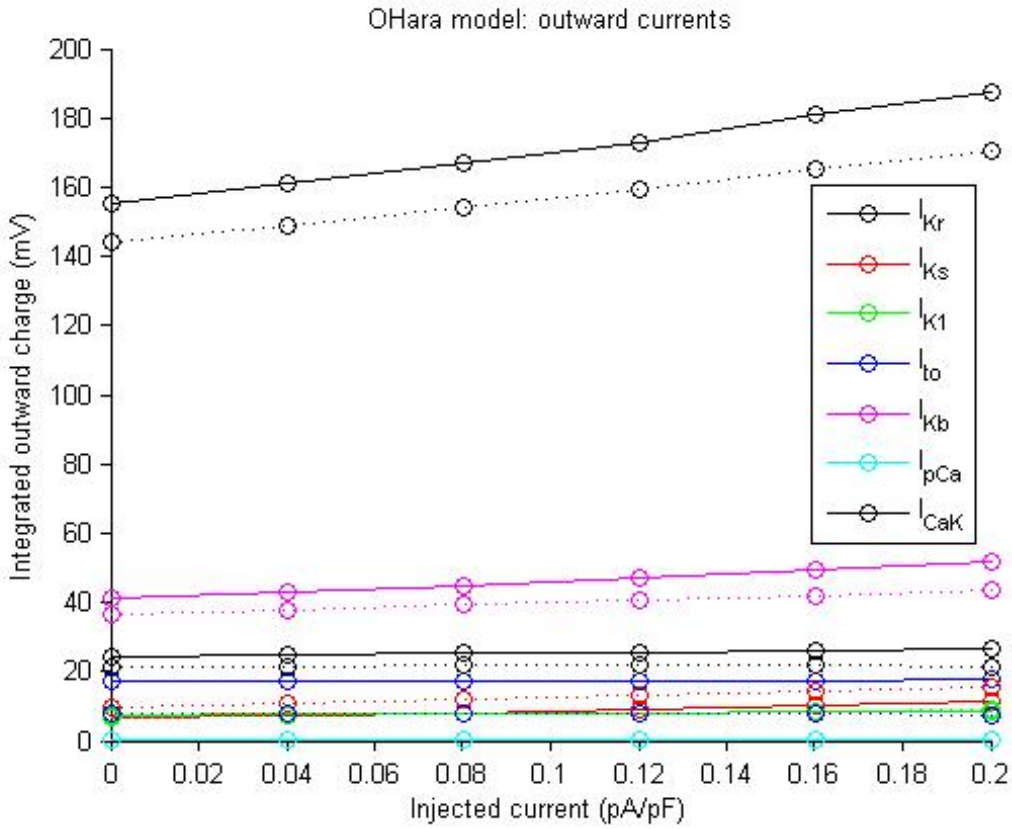

Figure 4.35: Integrated outward currents changed by current injected. Dotted lines represent each column of matrix Q_{fast} at fast rate, whereas solid line represent each column of matrix Q_{slow} at slow rate.

Fig.4.36 shows the rate-dependence of integrated currents. Each bar is a column of $\Delta\Delta Q$ matrix calculated by equation 3.1.

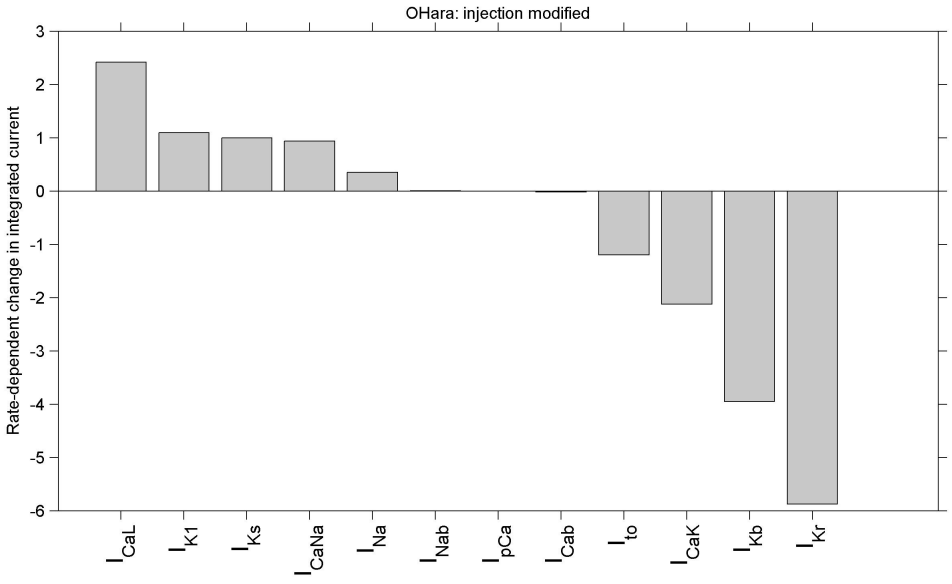

Figure 4.36: Rate-dependence of integrated currents influenced by current injected modified.

Chapter 5

Conclusions

Mathematical modeling is a powerful tool to investigate into biological systems, specially in physiology. In the last 50 years cardiac electrophysiology has become a fundamental discipline in the study of cardiac cells coupled with integrative modeling. Therefore, the aim of this research was to employ mathematical modeling for study how a perturbation of some conductance could influence ionic currents and AP shape and if this influence could be forward rate-dependent, reverse rate-dependent, or rate-independent.
To achieve this goal I used the O'Hara model, a modern mathematical model employed for understanding the basic mechanisms of ventricular arrhythmias at the level of ion channel currents and the single myocyte AP. Multivariable regression analysis was applied to study parameters sensitivity of the model and to evaluate their rate-dependence. Thereafter, regression analysis results were tested with two most varied parameters: one for the RRD (G_{Kr}) and one for the FRD (P_{NaK}). Perturbing the model with these conductances, a new method was applied to analyze how this perturbation influenced the other ionic currents. Through this new method, where a new matrix $\Delta\Delta Q$ was created, it was possible to figure out if the ionic currents were forward-dependent, reverse-dependent or rate-independent.
To clarify these disturbances effect, I considered two repolarization end-time of currents integration, first with different end-time and than with same end-

time. The idea was to investigate on ionic currents behavior during all the AP or without the total repolarization.
In the last stage, the Zaza's hypothesis was tested. His idea of "intrinsic reverse rate-dependence" was that shorter APs (at fast rates) will have faster rates of repolarization, and therefore, by injecting a current, this will have a smaller effect at a faster rate compared with that of a slower rate.

In conclusion, regression analysis has proven to be an excellent method to predict parameters model. Given the nonlinearities in the electrophysiology models, linear regression models can have strong predictive power. In previous works other models (e.g. Lou & Rudy1, Fox et al. and Kurata models [20]) were studied producing great results; here I confirmed its usefulness in the O'Hara model.
Test of two conductances confirmed the regression analysis prediction: G_{Kr} is reverse rate-dependent, whereas P_{NaK} is forward rate-dependent.
The idea of using a different end-time of repolarization has not delivered the desired results. There are no substantial differences in the AP shapes; only some ionic currents show small variations (I_{NaK}, I_{NaL} and I_{K1}).
Matrix $\Delta\Delta Q$ is a new method to evaluate the dynamic interplay between action potential and ionic currents after a specific perturbation. Through this new way, it is easier to understand if the influence of ionic currents and AP shape is forward rate-dependent, reverse rate-dependent, or rate independent and, subsequently, to plot them.
Zaza's hypothesis is largely confirmed: at slower rate, if I inject a current, there is a bigger influence in the APD than at faster rate. Nevertheless, I have not made much progress on this point.

Future Developments In this study I investigated only the O'Hara model behavior. As the regression analysis result could be different between different models, it would be of great interest if other mathematical models were tested.
The description of the electrophysiological effects of a perturbation by the

new matrix $\Delta\Delta Q$ is a great method to investigate the rate-dependence of each ionic current; however, in this work, there is no distinction between inward and outward current. Since it is well known that their behavior determines completely opposite effects, it should be improved considering this distinction.

Further, it is well known that intracellular Ca^{2+} dynamics of cardiac myocytes are regulated by complex mechanisms of a variety of ion channels, transporters, and exchangers. Alterations of these Ca^{2+} regulatory components might lead to development of cardiac diseases. It should be interesting to investigate the regulatory mechanisms and hidden Ca^{2+} dynamics using regression analysis and, especially, matrix $\Delta\Delta Q$, evaluating the effect of an eventual perturbation.

Bibliography

[1] LM Hondeghem and DJ Snyders: *Class III antiarrhythmic agents have a lot of potential but a long way to go. Reduced effectiveness and dangers of reverse use dependence.* Circulation 1990, 81:686-690.

[2] Tamas Banyasz, Balazs Horvath, Laszlo Virag, Laszlo Barandi, Norbert Szentandrassy, Gabor Harmati, Janos Magyar, Stefano Marangoni, Antonio Zaza, Andras Varro, and Peter P. Nanasi: *Reverse rate dependency is an intrinsic property of canine cardiac preparations.* Cardiovascular Research (2009) 84, 237-244.

[3] Antonio Zaza: *Control of the cardiac action potential: The role of repolarization dynamics.* Journal of Molecular and Cellular Cardiology 48 (2010) 106-111.

[4] Laszlo Barandi, Laszlo Virag, Norbert Jost, Zoltan Horvath, Istvan Koncz, Rita Papp, Gabor Harmati, Balazs Horvath, Norbert Szentandrassy, Tamas Banyasz, Janos Magyar, Antonio Zaza, Andras Varro, Peter P. Nanasi: *Reverse rate-dependent changes are determined by baseline action potential duration in mammalian and human ventricular preparations.* Basic Res Cardiol (2010) 105:315-323.

[5] Paul Dorian and David Newman: *rate-dependence of the effect of antiarrhythmic drugs delaying cardiac repolarization: an overview.* Europace (2000) 2, 277-285.

[6] Nerbonne, J. M. and Kass, R. S: *Molecular physiology of cardiac repolarization.* Physiological Reviews, 85, 1205-1253.

[7] Gui-Rong Li and Ming-Qing Dong: *Pharmacology of cardiac potassium channels.* Advances in Pharmacology, Volume 59, 1054-3589/10

[8] Eleonora Grandi, Francesco S. Pasqualini, Donald M. Bers: *A novel computational model of the human ventricular action potential and Ca transient.* Journal of Molecular and Cellular Cardiology 48 (2010) 112-121

[9] Petsy Pui-Sze So et al: *Blockade of IKs by HMR 1556 increases the reverse rate-dependence of refractoriness prolongation by dofetilide in isolated rabbit ventricles.* British Journal of Pharmacology (2006) 148, 255-263.

[10] Winslow et al: *Integrative modeling of the cardiac ventricular myocyte.* 2010 John Wiley & Sons, Inc. WIREs Syst Biol Med 2011 3 392-413

[11] Paul Dorian and David Newman: *Rate dependence of the effect of antiarrhythmic drugs delaying cardiac repolarization: an overview.* Europace (2000) 2, 277-285

[12] Sung-Young Shin et al: *Cardiac systems biology and parameter sensitivity analysis: intracellular Ca2+ regulatory mechanisms in mouse ventricular myocytes.* Adv Biochem Engin/Biotechnol (2008) 110: 25-45

[13] András Varró et al: *Theoretical possibilities for the development of novel antiarrhythmic drugs.* Current Medicinal Chemistry, 2004, 11, 1-11

[14] Hervé Abdi: *Partial least squares regression and projection on latent structure regression (PLS Regression).* 2010 John Wiley & Sons, Inc. WIREs Comp Stat

[15] Sanguinetti MC & Jurkiewicz NK (1990): *Two components of cardiac delayed rectifier K+ current. Differential sensitivity to block by class III antiarrhythmic agents.* J Gen Physiol 96, 195-215.

[16] Cheng, J.H. & Kodama, I. (2004): *Two components of delayed rectifier K+ current in heart: molecular basis, functional diversity and contribution to repolarization.* Acta Pharmacol. Sin., 25, 137-145.

[17] Li et al. (1996): *Evidence for two components of delayed rectifier K+ current in human ventricular myocytes.* Circ. Res., 78, 689.

[18] Hondeghem, L.M. & Snyders, D.J. (1990): *Class III antiarrhythmic agents have a lot of potential but a long way to go. Reduced effectiveness and dangers of reverse use dependence.*Circulation, 81, 686-690.

[19] Dorian, P. & Newman, D. (2000): *Rate dependence of the effect of antiarrhythmic drugs delaying cardiac repolarization: an overview.* Europace, 2, 277-285.

[20] Eric A. Sobie: *Parameter sensitivity analysis in electrophysiological models using multivariable regression.* Biophysical Journal, Volume 96.

[21] Amrita X. Sarkar, Eric A. Sobie (2010): *Regression analysis for constraining free parameters in electrophysiological models of cardiac cells.* PLoS Comput Biol 6(9): e1000914.

[22] Amrita X. Sarkar, PhD, Eric A. Sobie: *Quantification of repolarization reserve to understand interpatient variability in the response to proarrhythmic drugs: A computational analysis.* 2011 Heart Rhythm Society.

[23] Abdallah Mashal et al: *atrial Fibrillation: a Primary care cross-sectional study.* IMAJ 2011; 13: 666-671

[24] O'Hara T, Virág L, Varró A, Rudy Y (2011): *Simulation of the undiseased human cardiac ventricular action potential: model formulation and experimental validation.* PLoS Comput Biol 7(5): e1002061.

[25] Clancy CE, Rudy Y (1999) *Linking a genetic defect to its cellular phenotype in a cardiac arrhythmia.* Nature 400: 566569.

[26] Silva J, Rudy Y (2005): *Subunit interaction determines IKs participation in cardiac repolarization and repolarization reserve.* Circulation 112: 13841391.

[27] Hund TJ, Rudy Y (2004): *Rate dependence and regulation of action potential and calcium transient in a canine cardiac ventricular cell model.* Circulation 110: 3168-3174.

[28] Heijman J, Volders PG, Westra RL, Rudy Y (2011): *Local control of beta- adrenergic stimulation: effects on ventricular myocyte electrophysiology and Ca(2+)-transient.* J Mol Cell Cardiol 50: 863871.

[29] Saucerman JJ, Healy SN, Belik ME, Puglisi JL, McCulloch AD (2004): *Proarrhythmic consequences of a KCNQ1 AKAP-binding domain mutation: computational models of whole cells and heterogeneous tissue.* Circ Res 95: 1216-1224.

[30] Puglisi JL, Wang F & Bers DM (2004): *Modeling the isolated cardiac myocyte.* Progress in Biophysics & Molecular Biology 85(2-3): 163-178.

[31] Winslow RL, Cortassa S & Greenstein JL (2005): *Using models of the myocyte for functional interpretation of cardiac proteomic data.* Journal of Physiology-London 563(1): 73-81.

[32] Hodgkin AL & Huxley AF (1952): *A quantitative description of membrane current and its application to conduction and excitation in nerve.* J Physiol 117(4): 500-44.

[33] Noble D (1962): *A modification of the Hodgkin–Huxley equations applicable to Purkinje fibre action and pace-maker potentials.* J Physiol 160: 317-52.

[34] Han CL, Tavi P & Weckstrom M (2002a): *Modulation of action potential by [Ca2+](i) in modeled rat atrial and guinea pig ventricular myocytes.* American Journal of Physiology-Heart and Circulatory Physiology 282(3): H1047-H1054.

[35] ten Tusscher KHWJ, Noble D, Noble PJ & Panfilov AV (2004): *A model for human ventricular tissue.* American Journal of Physiology-Heart and Circulatory Physiology 286(4): H1573-H1589.

[36] Shannon TR, Wang F, Puglisi J, Weber C & Bers DM (2004) *A mathematical treatment of integrated Ca dynamics within the ventricular myocyte.* Biophysical Journal 87(5): 3351-3371.

[37] Keener J & Sneyd J (1998): *Mathematical physiology.* Springer, New York.

[38] Dulhunty AF (2006): *Excitation-contraction coupling from the 1950s into the new millennium.* Clinical and Experimental Pharmacology and Physiology 33(9): 763-772.

[39] Beeler GW & Reuter H (1977): *Reconstruction of the action potential of ventricular myocardial fibres.* J Physiol 268(1): 177-210.

[40] DiFrancesco D & Noble D (1985): *A model of cardiac electrical activity incorporating ionic pumps and concentration changes.* Philos Trans R Soc Lond B Biol Sci 307(1133): 353-98.

[41] Stern MD (1992): *Theory of excitation-contraction coupling in cardiac-muscle.* Biophysical Journal 63(2): 497-517.

[42] Luo C, Rudy Y. 1991: *A model of the ventricular cardiac action potential: depolarization, repolarization and their inter- action.* Circ. Res. 68:1501-26

[43] Luo C, Rudy Y. 1994: *A dynamic model of the cardiac ventricular action potential: simulations of ionic currents and concentration changes.* Circ. Res. 74(6):1071-96

[44] Noble D, Varghese A, Kohl P, Noble P. 1998: *Improved guinea-pig ventricular cell model incorporating a diadic space, iKr and iKs, and length- and tension-dependent processes.* Can. J. Cardiol. 14(1):123-34

[45] Rashmi R. Shah, Luc M. Hondeghem:*Refining detection of drug-induced proarrhythmia: QT interval and TRIaD.* Heart Rhythm 2005; 2:758-772)

[46] Clive Orchard and Fabien Brette: *t-tubules and sarcoplasmic reticulum function in cardiac ventricular myocytes.* Cardiovascular Research (2008) 77, 237-244

[47] Luc M. Hondeghem: *Thorough QT/QTc not so thorough: removes torsadogenic predictors from the T-wave, incriminates safe drugs, and misses profibrillatory drugs.* J Cardiovasc Electrophysiol, Vol. 17, pp. 337-340, March 2006.

[48] Luc M. Hondeghem: *Relative contributions of TRIaD and QT to proarrhythmia.* J Cardiovasc Electrophysiol, Vol. 18, pp. 655-657, June 2007.

[49] Sung-Young Shin, Sang-Mok Choo, Sun-Hee Woo, Kwang-Hyun Cho: *Cardiac systems biology and parameter sensitivity analysis: intracellular Ca2+ regulatory mechanisms in mouse ventricular myocytes* Adv Biochem Engin/Biotechnol (2008) 110: 25-45.

[50] McAllister RE, Noble D, Tsien RW (1975): *Reconstruction of the electrical activity of cardiac Purkinje fibres.* J Physiol 251:1

[51] Saltelli A, Ratto M, Tarantola S, Campolongo F (2005): Sensitivity analysis for chemical models Chem Rev 105:2811

[52] Zhang Y, Rundell A (2006): Dynamic modelling and analysis of biochemical networks: mechanism-based models and model-based experiments. IEE Proc Syst Biol 153:201

[53] Schwacke JH, Voit EO (2005) Concentration-dependent effects on the rapid and efficient activation of the MAP kinase signaling cascade. J Theor Biol 236:21

[54] Roger G. Mark (2004): Principles of cardiac electrophysiology. pages 115-126

[55] Marenco, JP et al: Improving Survival from Sudden Cardiac Arrest. The Role of the Automated External Defibrillator. JAMA. 2001;285:1193-1200

[56] Smye SW, Clayton RH: Mathematical modelling for the new millennium: medicine by numbers. Med Eng Phys. 2002;24: 565-74.

[57] Rudy Y: From genetics to cellular function using computational biology. Ann NY Acad Sci. 2004;1015:261-70.

[58] Nash MP, Panfilov AV: Electromechanical model of excitable tissue to study reentrant cardiac arrhythmias. Prog Biophys Mol Biol. 2004;85:501-22.

Appendix A

ORd Human Model Basic Parameters

Table A.1: Model kinetic parameters varied in O'Hara model

Parameter	Definition
p_m	Na^+ current activation time constant
p_{hFast}	Na^+ current fast inactivation time constant
p_{hSlow}	Na^+ current slow inactivation time constant
p_j	Na^+ current fast inactivation time constant
p_{hL}	Na^+ current late activation time constant
p_a	I_{to} current activation time constant
p_{iFast}	I_{to} current fast inactivation time constant
p_{iSlow}	I_{to} current slow inactivation time constant
p_{fFast}	I_{CaL} current fast voltage dependent inactivation time constant
p_{fSlow}	I_{CaL} current slow voltage dependent inactivation time constant
$p_{fCaFast}$	I_{CaL} current fast development of Ca^{2+} dependent inactivation time constant
$p_{fCaSlow}$	I_{CaL} current slow development of Ca^{2+} dependent inactivation time constant
p_{jCa}	I_{CaL} current recovery from Ca^{2+} dependent inactivation time constant
p_{xrFast}	I_{Kr} current fast activation/deactivation time constant
p_{xrSlow}	I_{Kr} current slow activation/deactivation time constant
p_{xS1}	I_{Ks} current activation time constant
p_{xS2}	I_{Ks} current deactivation time constant
p_{xK1}	I_{K1} current inactivation time constant

Table A.2: Model maximal ionic conductances varied in O'Hara model

Parameter	Definition
G_{na}	Maximal Na^+ conductance
G_{NaL}	Maximal Ca^{2+} conductance through the L-type Ca^{2+} channel
G_{to}	Maximal transient outward K^+ conductance
G_{kr}	Maximal rapid delayed rectifier K^+ conductance
G_{ks}	Maximal slow delayed rectifier K^+ conductance
G_{K1}	Maximal inward rectifier K^+ conductance
G_{ncx}	Maximal total Na^+/Ca^+ exchange conductance
G_{kb}	Maximal K^+ background conductance
G_{pCa}	Maximal sarcolemmal Ca^{2+} pump conductance
P_{ca}	Maximal permeability to ion Ca^{2+}
P_{nak}	Maximal Na^+/Ca^{2+} exchange conductance
P_{nab}	Maximal Na^+ background conductance
P_{cab}	Maximal Ca^{2+} background conductance

Table A.3: Model voltage dependences of activation and inactivation varied in O'Hara model.

Parameter	Definition
$Vshift_m$	Na^+ current activation
$Vshift_h$	Na^+ current fast inactivation
$Vshift_{mL}$	Late Na^+ current activation
$Vshift_{hL}$	Late Na^+ current inactivation
$Vshift_a$	I_{to} current activation
$Vshift_d$	L-type Ca^{2+} current activation
$Vshift_f$	L-type Ca^{2+} current voltage-dependent inactivation
$Vshift_{xr}$	Rapid delayed rectifier K^+ current activation
$Vshift_{xs1}$	Slow delayed rectifier K^+ current activation
$Vshift_{k1}$	Inward rectifier K^+ current voltage-dependent block/rectification

Appendix B

APs comparison at different basic cycle length

In order to give a look to the behavior of the O'Hara model, the AP shape was plotted at 7 different BCL. From 300 ms to 5000 ms. Result is shown in Fig. B.1.

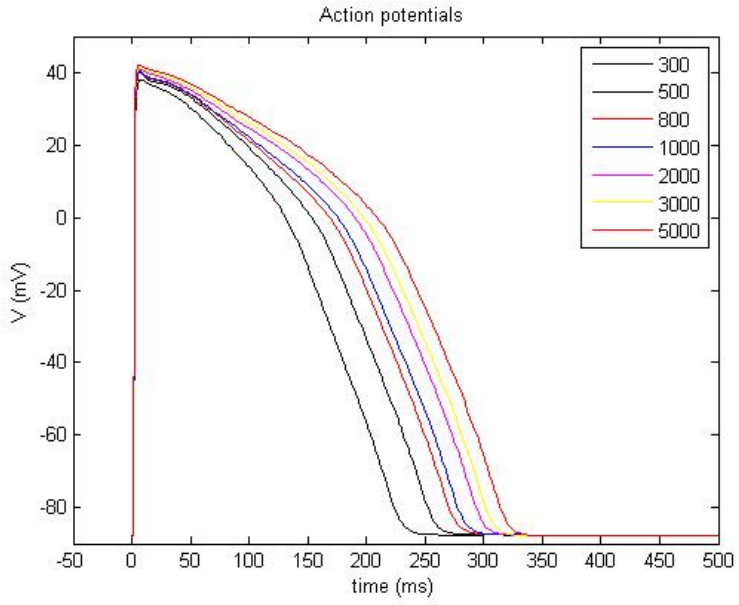

Figure B.1: APs comparison at different basic cycle length obtained with the O'Hara model.

Appendix C

G_{Ks} perturbation results

G_{ks} was perturbed by a scale factor e^x, where x is a vector varied from 0 to -2 by a step of 0.25. Fig.C.1 shows the FRD of G_{Ks}. The effect at slow rate (solid line) is smaller than at fast rate (dotted line).

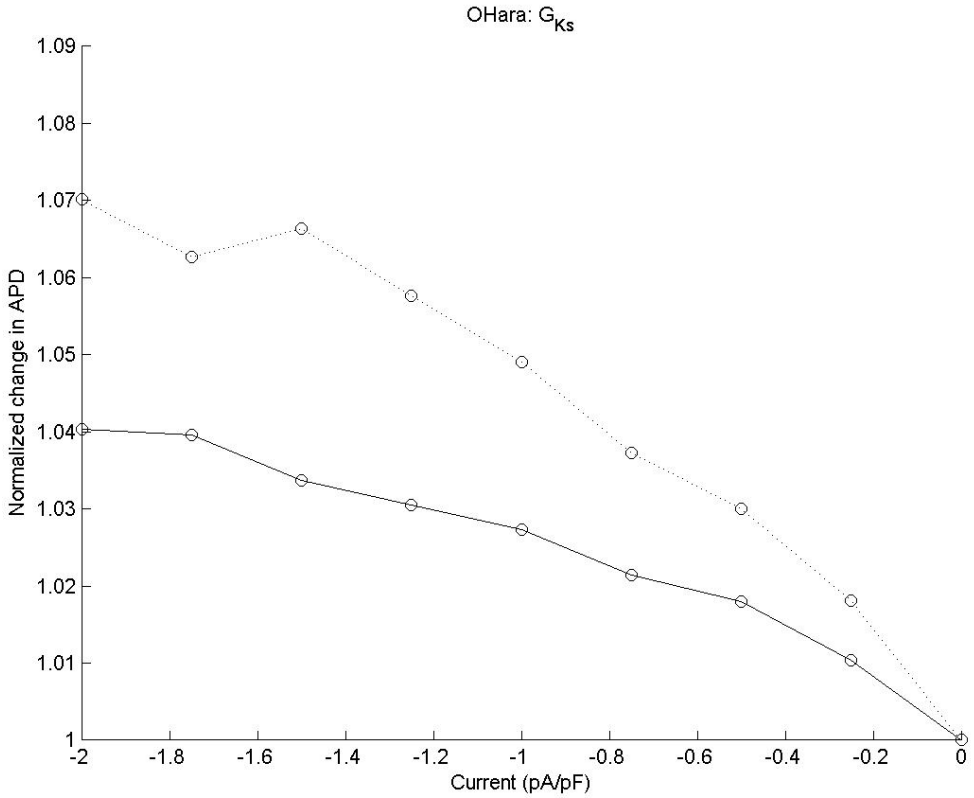

Figure C.1: Effect of G_{Ks} modified on APD normalized. Plot confirms that at slow rate (solid line) has a smaller effect than at fast rate (dotted line). G_{Ks} is FRD.

Fig.C.2 shows the result for the inward currents, whereas Fig.C.3 shows the result for the outward currents. Each current is plotted at fast rate (dotted line) and at slow rate (solid line).

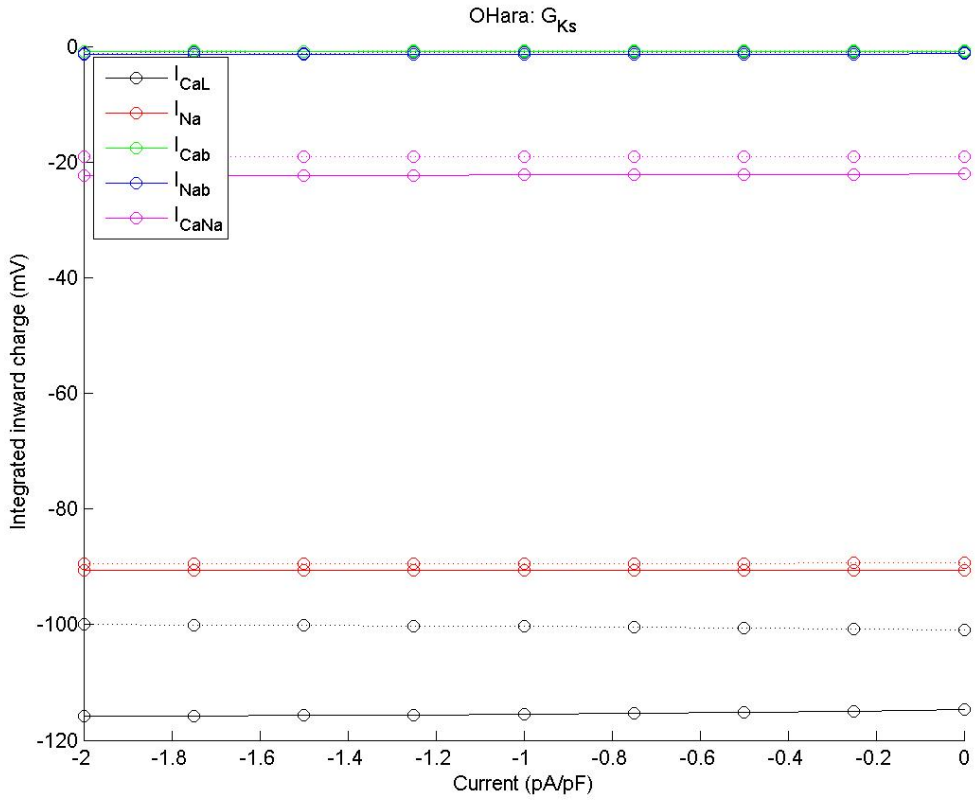

Figure C.2: Integrated inward currents changed by G_{Ks}. Dotted lines represent each column of matrix Q_{fast} at fast rate, whereas solid line represent each column of matrix Q_{slow} at slow rate.

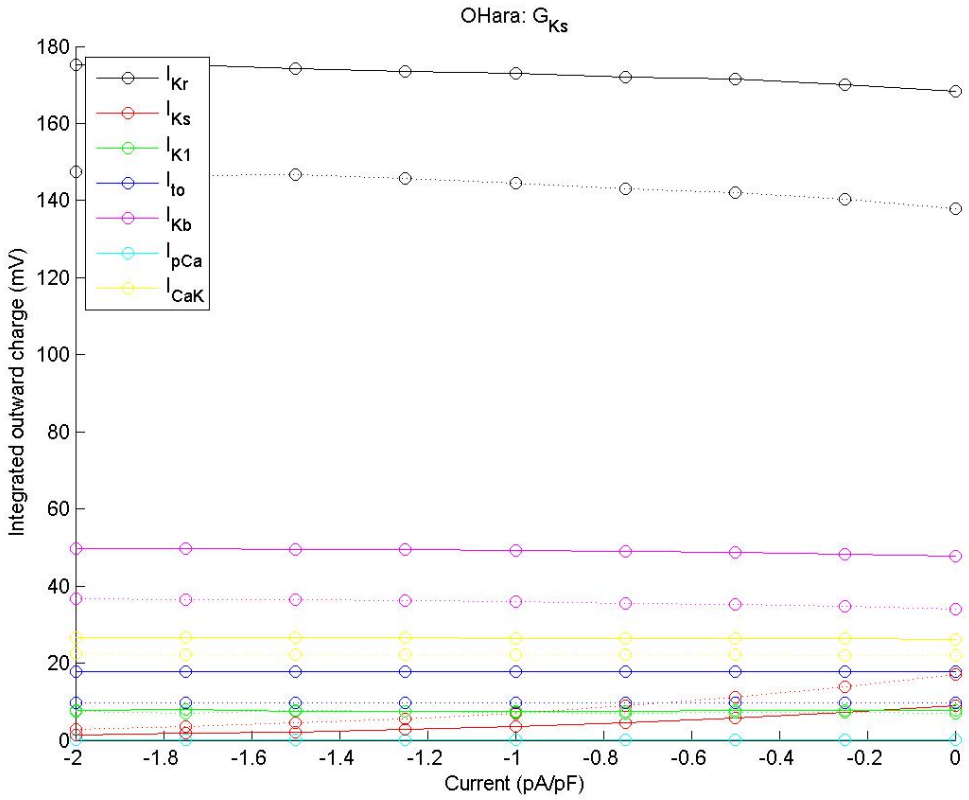

Figure C.3: Integrated outward currents changed by G_{Ks}. Dotted lines represent each column of matrix Q_{fast} at fast rate, whereas solid line represent each column of matrix Q_{slow} at slow rate.

Fig. C.4 shows the rate-dependence of integrated currents. Each bar is a column of $\Delta\Delta Q$ matrix calculated by equation 3.1.

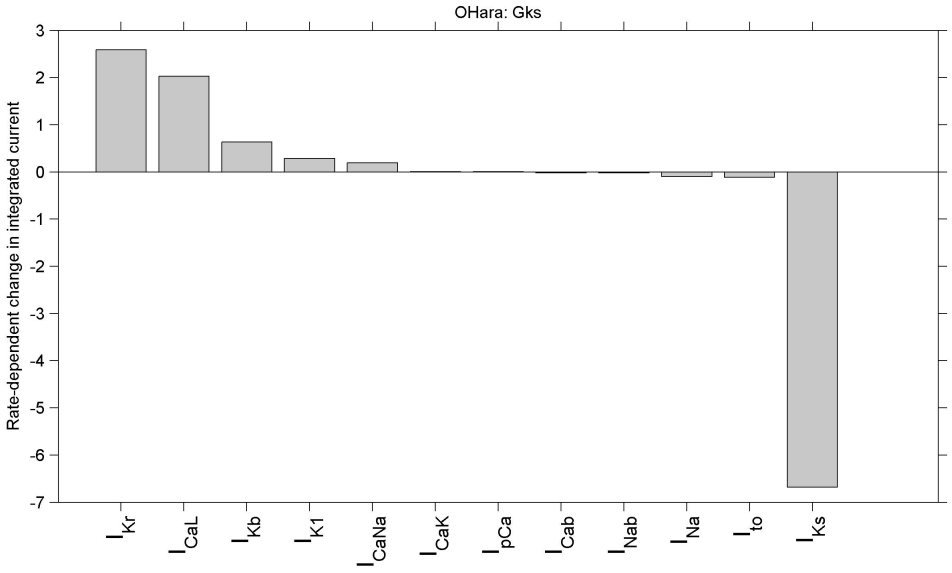

Figure C.4: Rate-dependence of integrated currents influenced by G_{ks}.